COHERENT STRUCTURES IN TURBULENT FLOWS:

EXPERIMENTAL STUDIES ON THE TURBULENCE OF

MULTIPHASE PLUMES AND TIDAL VORTICES

A Dissertation

by

DUNCAN BURNETTE BRYANT

Submitted to the Office of Graduate Studies of
Texas A&M University
in partial fulfillment of the requirements for the degree of

DOCTOR OF PHILOSOPHY

May 2010

Major Subject: Ocean Engineering

COHERENT STRUCTURES IN TURBULENT FLOWS:

EXPERIMENTAL STUDIES ON THE TURBULENCE OF

MULTIPHASE PLUMES AND TIDAL VORTICES

A Dissertation

by

DUNCAN BURNETTE BRYANT

Submitted to the Office of Graduate Studies of
Texas A&M University
in partial fulfillment of the requirements for the degree of

DOCTOR OF PHILOSOPHY

Approved by:

Chair of Committee,	Scott A. Socolofsky
Committee Members,	Yassin A. Hassan
	James Kaihatu
	Kuang-An Chang
Head of Department,	John Niedzwecki

May 2010

Major Subject: Ocean Engineering

ABSTRACT

Coherent Structures in Turbulent Flows: Experimental Studies on the Turbulence of

Multiphase Plumes and Tidal Vortices. (May 2010)

Duncan Burnette Bryant, B.S., Clemson University;

M.S., Clemson University

Chair of Advisory Committee: Dr. Scott A. Socolofsky

This dissertation presents the turbulence of multiphase plumes and tidal vortices by studying and quantifying coherent structures that affect the dynamics of the flow. The measurements presented in this dissertation were taken using particle image velocimetry (PIV). After preprocessing the images and conducting the PIV analysis to get the final velocity fields, the local swirl strength was used to identify coherent structures (vortices) in the flow. This dissertation used the identified vortices to quantify the turbulent properties of the flows.

The mean and turbulent properties of bubble plumes are found to be self-similar within the measured air flow rates when appropriately nondimensionalized. The time-averaged velocity profile was shown to have a Gaussian distribution when nondimensionalized by the centerline velocity and plume radius. The bubble plumes were found to have the most energetic vortices along the plume edge and a modulated turbulent energy spectrum with a slope in the inertial subrange from -7/6 instead of the classical -5/3.

The mean and turbulent properties of an inertial particle plume are presented, revealing the time-averaged velocity and vorticity profiles to be self-similar for all cases when nondimesionalized by the centerline velocity and plume radius. The average vortex properties were not self-similar for all flow cases with the largest two particles sizes being self-similar and the smallest particle vortex properties being similar to bubble plume data. Despite the difference in vortex properties, the turbulent energy spectra in inertial particle plumes followed the same modulation as the bubble plumes.

PIV experiments from the tidal starting-jet vortices detail the influence of a finite channel length using identified vortice. The results show the trajectory and development of the tidal starting-jet vortices to be changed by a region of vorticity that develops inside the channel and is expelled as a vortex during the ebb tide. This expelled lateral boundary layer vortex is shown to move the starting-jet vortex away from the tidal jet shear layer thus reducing the input vorticity. When the expelled boundary layer vortex strength is 1/5 the starting-jet vortex the system dynamics change resulting in a deviation in the starting-jet vortices' trajectory.

This dissertation successfully uses the local swirl strength to quantify the turbulence of multiphase plumes and tidal starting-jet vortices. Using these results, engineers will be able to better predict the efficiency of CO_2 ocean sequestration and tidal flushing. Furthermore, the techniques of quantifying coherent structures developed in this dissertation can be applied to a multitude of turbulent flows.

DEDICATION

This dissertation is first dedicated to my parents, whose love and support were critical in its completion. Secondly, this dissertation is dedicated to my brothers, Jason and Josh, whose own desires to learn and succeed showed me the path. Finally, this dissertation is dedicated to my grandmother Nelson, whose strength and will I aspire to emulate.

ACKNOWLEDGEMENTS

I would like to first thank my advisor, Dr. Scott Socolofsky, for his time, leadership and dedication. His example as a teacher, advisor, and mentor, I will carry with me throughout my career and his commitment to teaching and research was an inspiration. I would like to thank the rest of my committee members, Dr. Chang, Dr. Kaihatu, and Dr. Hassan, for their guidance and support throughout the course of this research.

Thanks go to my research mate, Dr. Dong-Guan Seol, who helped me to learn the laboratory methods used in this dissertation and aided in my initial understanding of PIV processing. I would like to thank Mr. John Reed for his guidance in the lab, and Professor Jirka for access to the shallow water basin at the University of Karlsruhe, Institute of Hydromechanics. I would like to thank my classmates, officemates, and friends for their encouragement and for making my time at Texas A&M a wonderful and fulfilling experience. Lastly, I would like to thank my family who support and love are unwavering.

NOMENCLATURE

D	Characteristic Plume Length Scale
$d^{2\text{-}D}$	Two-dimensional Velocity Gradient Tensor
Fr	Froude Number
g	Gravitational Constant
K_w	Inlet Strouhal Number
L	Channel Length
L_1	Integral Length Scale
l_j	Jet Excursion Length Scale
l_s	Sink Length Scale
Q_g	Volumetric Air Flow Rate
r	Plume Radius
Re	Reynolds Number
T	Tidal Period
t	Time
U	Maximum Inlet Velocity
u	Horizontal Velocity
v	Vertical Velocity
v_c	Centerline Vertical Velocity
$\overline{v'^2}$	Reynolds Stress
W	Inlet Width

w_b	Slip Velocity
x	Horizontal Direction
y	Vertical Direction
α	Entrainment Coefficient
Γ	Circulation
Γ_E	Circulation in Boundary Layer
Γ_S	Starting-jet Circulation
δ	Boundary Layer Width
ε	Dissipation
η	Kolmogorov Length Scale
λ	Ratio of the Dispersed Phase and Continuous Phase Radii
ν	Viscosity
χ	Local Void Fraction
ω	Vorticity

TABLE OF CONTENTS

LIST OF FIGURES

LIST OF TABLES

CHAPTER I

INTRODUCTION

1.1 Problem Statement

Environmental flows have become increasingly important to engineers as topics such as global warming, water quality and air pollution have emerged as important worldwide issues. As the need for a greater understanding of environmental flows becomes paramount, knowledge of the dynamic role of turbulence in mixing is also necessary. Turbulence is often defined by its symptoms which include, enhanced mixing, vorticity, and chaotic in nature (Tennekes and Lumley 1972). Due to the chaotic nature of turbulence, statistical temporal methods such as Reynolds decomposition and spectral analysis have been used to understand turbulent flows (Pope 2000). While these methods have aided the understanding of environmental flows, they are not able to describe the entire flow field simultaneously, making it difficult to understand the system dynamics. With the advent of methods such as particle image velocimetry (PIV) (Raffel et al. 1998), spatial data has become increasingly more available to explain complex fluid flows. Using velocity fields resulting from PIV, the identification of coherent turbulent structures in the flow has become an active area of rising interest (Adrian et al. 2000). The understanding of coherent turbulent structures in fluid flows allows engineers to visualize the flow and distinguish parameters responsible for mixing.

_____

This dissertation follows the style and format of *Journal of Hydraulic Engineering*.

Coherent structures can be defined as characteristic recurrent forms in turbulent flows (Holmes et al. 1996). Examples of coherent structures include counter-rotating vortices in the wake of flow past structures, burst in turbulent boundary layers, and vortices forming in shear layers. Often coherent structures are formed due to an instability in the flow including Tollmien-Schlichting instabilities or Kelvin-Helmholtz instabilities (Holmes et al. 1996). The most common turbulent coherent structures refer to vortices in the flow. Thus by understanding vortices in the flow including their size and strength an understanding of the coherent structures in the flow is realized. Currently, methods such as proper orthogonal decomposition (POD) aid in the identification of coherent structures in resulting PIV velocity fields (Meyer et al. 2007). Multiphase plumes and tidal vortices vary greatly in scale, but the identification of coherent turbulent structures can be successfully applied to understand the dynamics of these flows.

Multiphase plumes, driven by air bubbles (Tekeli and Maxwell 1978; Milgram 1983) or inertial particles, are important for mixing in reservoirs (McGinnis et al. 2004), loop reactors (Díaz et al. 2006; Buwa and Ranade 2002; Mudde and Van Den Akker 1999), and ocean CO_2 sequestration (Adams and Wannamaker 2005; Adams and Wannamaker 2006). In particular, ocean CO_2 sequestration has been noted by the Intergovernmental Panel on Climate Change in its 2005 special report on Carbon Dioxide Capture and Storage as a method to successful storage CO_2 for centuries (Metz et al. 2005). The report specifically acknowledges the need for engineers to determine the most efficient and cost-effective way of running an ocean CO_2 sequestration operation. The efficiency of delivering CO_2 into the ocean depends on the mixing which is related to the

turbulence.   By conducting experiments and studying the turbulence of multiphase plumes using vortex identification this dissertation gives engineers and scientist the knowledge to validate models and develop design tools.

Tidal vortices play an important role in mixing in coastal waters and estuaries (Van Senden and Imberger 1990). The transport of sediment, fish larva, and pollutants in and out of estuaries are impacted by these tidal vortices. To understand the large turbulent structures, it is important to have high quality spatial data which can be used to identify and characterize them in the flow. This dissertation contributes to the knowledge of tidal starting-jet vortices by conducting a physical model test to determine the impact a channel of finite length (jetties or increased barrier island width) has on the trajectory and strength of these structures.

In short, this dissertation uses vortex identification by method of the swirl strength criterion (Adrian et al. 2000) to successfully describe the turbulence of multiphase plumes and tidal vortices, furthering the development of vortex identification and quantification, relating spatial and temporal turbulent analysis methods, and providing details on these flows which have far reaching implications in the fields of multiphase flows, environmental fluid mechanics, and ocean and coastal engineering.

1.2 Literature Review

1.2.1 State of Knowledge for Bubble Plumes and Inertial Particle Plumes

Jets and plumes are highly turbulent flows leading to efficient mixing in both industrial applications and environmental settings. Bubble plumes, driven by the buoyancy of the

dispersed bubble phase (Tekeli and Maxwell 1978; Milgram 1983), are used in reservoir management (McGinnis et al. 2004), loop reactor mixing (Díaz et al. 2006; Buwa and Ranade 2002; Mudde and Van Den Akker 1999), and have implications as a method for CO_2 sequestration (Adams and Wannamaker 2005; Adams and Wannamaker 2006). Though bubble plumes are common in industry and environmental flows, the turbulent properties of continuous phase (water) are difficult to measure because of the dispersed phase (bubbles, droplets, or sediment).

Previous studies of bubbles plumes used acoustic Doppler velocimeters (García and García 2006) and laser Doppler anemometers (Mudde and Van Den Akker 1999; Becker et al. 1999) to measure velocities near the plumes, but were unable to make measurements inside the plumes due to the dispersed phase. Particle image velocimetry (PIV) was used successfully by Seol et al. (2007) and Simiano et al. (2006) to measure mean flow properties of the bubble plume's interior by removing or separating the dispersed phase. However, these studies did not quantify turbulent characteristics, such as the integral length scale, vortex size, and vortex circulation. Buscaglia et al. (2002) and Bombardelli et al. (2003) clearly demonstrated the differences in mass transport associated with a one dimensional integral plume model compared to an unsteady Reynolds average Navier-Stokes simulation using a k-ε model or large eddy simulation approach. This difference in mass transport stems from the inability of the integral model to correctly account for enhanced mixing due to turbulence. Furthermore, Lance and Bataille (1991), Shawkat et al. (2007), and Rensen et al. (2005) clearly show a

dissipation rate of -5/3 is not followed in bubbly pipe flow, thus changing the relationship between turbulent production and dissipation.

Often bubble plumes are operating in a stratified ambient, such as a reservoir or ocean environment. The introduction of stratification greatly increases the complexity of the buoyant bubble plume with the creation of a downward, negatively buoyant outer plume. Bubble plumes in a stratified ambient are often represented by the one-dimensional integral plume model presented by Asaeda and Imberger (1993), which is dependent on an entrainment coefficient which linearly relates the plume centerline velocity to the entrainment velocity. The inner plume models the transfer of momentum to the entrained fluid by the bubbles. As this fluid rises, it becomes negatively buoyant. When the buoyancy of the bubbles is insufficient to maintain the upward movement of fluid, the fluid peels away from the inner plume and begins to move downwards, creating the second outer plume. The outer plume moves downward until the fluid becomes neutrally buoyant at the trap height, where it spreads laterally.

Many studies have been conducted to find bulk properties such as the peel height and trap height of a bubble plume in stratification (McDougall (1978); Asaeda and Imberger (1993); Baines and Leitch (1992); Lemckert and Imberger (1993)); however, measurement techniques that can determine turbulent properties have not been conducted. Bubbles, the size of which are a function of the water surface tension, become much smaller in a stratified ambient due to the addition of salt to create stratification. PIV requires separation of the dispersed and continuous phase and is therefore difficult to employ.

1.2.2 State of Knowledge for Tidal Vortices

Estuaries and surrounding coastal systems are important for marine habitat, shipping, and recreation, and are often composed of complex fluid flows. These systems serve as the spawning and maturation sites for larval and young fish (Roughan et al. 2005), and are important in the dispersion of suspended nutrients and containments (Chadwick and Largier 1999a). One particular flow feature in inlet systems are starting-jet vortices that develop in response to tidal flows and impact estuary flushing (Van Senden and Imberger 1990).

Vortex dynamics in shallow-water flows have been extensively studied with both experimental and numerical methods. Since starting-jet vortices in shallow water have a horizontal length scale much greater than the water depth, they are classified as two-dimensional large coherent structures (Jirka 2001). The generation of a tidal vortex is formed by the flow separation from the lateral boundary, which transports high vorticity (Signel and Geyer 1991), or by the transport of vorticity from the inlet channel rolling up to create a vortex (Wells and van Heijst 2003).

Field studies of tidal vortices have been conducted using acoustic Doppler current profilers (ADCP) by Pawlak et al. (2003), Geyer and Signell (1990), Geyer (1993), and Old and Vennell (2001). Additionally, van Senden and Imberger (1990) used a conductivity, temperature, and depth (CTD) profiler in combination with drifters to study the growth and quasi-steady phase of tidal vortices. These studies identify tidal vortices and associated properties such as upwelling but are unable to acquire high spatial resolution data.

Numerical studies of ocean and coastal flows are often employed due to the difficulty of field experiments and scaling requirements for laboratory experiments. A numerical model study of flow around headlands using a depth-integrated vorticity equation was performed by Signell and Geyer (1991). Flow through an inlet is inherently different from flow around headlands because the produced vortex from an inlet has an identical, opposite rotating vortex across the channel that results in self-propagation by dipole formation (Wells and van Heijst, 2003). However, Signell and Geyer (1991) did demonstrate the successful implementation of a depth-integrated model to capture the flow of large two-dimensional coherent structures and the change in generation and propagation due to changes in three important length scales controlling the flow: frictional length, tidal excursion, and headland length.

Experiments conducted by Lin et al. (2003) studying starting-jet vortices formation in shallow water with a free surface boundary show the evolution of the vortex in time with varying water depth. This study also captured the three-dimensionality of large two-dimensional starting-jet vortices. Starting-jet vortices through an inlet have also been studied experimentally. Kashiwai (1985a, and 1985b) conducted large-scale experiments in a 5m by 5m basin and used floats to determine the qualitative flow pattern. Wells and van Heijst (2003) conducted dye experiments in a stratified fluid, thus minimizing bottom friction effects, and found three different tidal starting-jet vortex conditions exist based on the inlet Strouhal number, K_w, calculated as

$$K_w = \frac{W}{UT},$$ (1.1)

where W is the tidal inlet width, U is the maximum velocity through the inlet, and T is the tidal period. Type 1, characterized by the escape of tidal vortices from the reversing tide, occurs under conditions where $K_w < 0.13$. Type 2 ($K_w = 0.13$) results in a stationary dipole where self-propagation and the reversing tide's sink flow are equal; and Type 3 ($K_w > 0.13$) is the entrainment of the dipole back into the inlet. The inlet Strouhal number can be seen as the ratio of the sink length scale, l_s, to the jet excursion length scale, l_j. Furthermore, l_j was shown by Signell and Geyer (1991) to be

$$l_j = \frac{UT}{\pi} .$$ (1.2)

The length scale of the sink flow was expressed by Chadwick and Largier (1999b) as

$$l_s = \sqrt{\frac{UWT}{\pi^2}} .$$ (1.3)

Combining these two length scales, we find that

$$\frac{l_s}{l_j} = \sqrt{K_w} .$$ (1.4)

Substituting the critical value of $K_w = 0.13$ into the above equation results in a length scale ratio of 0.3606. Thus, the starting-jet vortices are drawn back into the inlet when

the characteristic jet length scale is less than 2.77 times the characteristic sink length scale. Further experiments by del Roure (2007) studied starting-jet vortices through idealized inlets using surface particle image velocimetry (PIV) with the presence of bottom friction. The resulting vector maps were used to identify vortices in the flow and quantify their trajectory, circulation and upwelling. These experiments confirmed that the inlet Strouhal number could be used to predict starting-jet vortex type with a fully developed bottom boundary layer.

Though previous studies have successfully predicted the flow pattern for idealized cases, these studies did not investigate the effect of an expelled lateral boundary layer on the generation and propagation of tidal starting-jet vortices. The lateral boundary layer forms in a tidal inlet during both the ebb and flood tide. This boundary layer has a region of recirculation, as shown in previous studies by Kashiwai (1985a) that is expelled out from the tidal inlet during the reverse flow. The rotation of this recirculation region is opposite that of the generated starting-jet vortex, resulting in a feature similar to that of a dipole.

1.3 Dissertation Organization

This dissertation follows the organization method of combining papers. In the following chapter, the results for PIV experiments of a bubble plume are presented with focus on the identification and analysis of vortices in the flow. This chapter also relates the results of temporal and spatial analysis. Chapter III uses PIV to quantify the mean and turbulent properties of inertial particle plumes. This chapter uses the methods developed in Chapter II and compares its results to the corresponding bubble plume data. Chapter

IV uses the vortex identification and quantification method developed in Chapter II to quantify the size, strength, and trajectory of large two-dimensional vortices associated with tidal flows through an inlet of finite length.

CHAPTER II

QUANTIFICATION OF TURBULENCE PROPERTIES IN BUBBLE PLUMES

USING VORTEX IDENTIFICATION METHODS[*]

Turbulence characteristics within bubble plumes are quantified in the laboratory using particle image velocimetry (PIV) data and post-processing techniques to identify continuous-phase vortices and their properties. Experiments are conducted using a single, high-speed Phantom camera (frame rate 250 Hz); images are pre-processed to eliminate signatures from the bubbles, resulting in high temporal and spatial resolution PIV data for the continuous phase only. The local swirl strength is used to identify vortices in the flow field. By combining the velocity fields and identified vortex maps, the vortex size probability distribution and the relationship of the vortex size, circulation and enstrophy with respect to the position in the plume are quantified. Results demonstrate that these quantities are self-similar when nondimensionalized by the plume radius and centerline velocity. A direct relationship is also identified between vortex size and the corresponding average circulation and enstrophy. Modulation of theturbulent energy spectrum compared to a single-phase plume is noted and is attributed to the presence of the bubbles in the flow. Vortex size and energy density are

greatest in the shear layers at the edge of the round plume, indicating that shear instability, and not bubble wakes, is the dominant process of large-scale turbulent and coherent structure generation in bubble plumes.

2.1 Introduction

Jets and plumes are common in nature and are applied in industry as a means of generating mixing, among other uses. A subset of these flows is multiphase plumes, which have grown in environmental interest as they have been used in lake destratification and aeration for water quality management. More recently, CO_2 droplet or CO_2 hydrate plumes for direct carbon sequestration in the oceans have been considered as a means to mitigate the effects on global warming of burning fossil fuels. While the concept of CO_2 sequestration is promising, the turbulent structures in multiphase plumes that control the instantaneous concentration field and local dilution are poorly understood. These coherent and vortical structures are particularly important in reservoir aeration and CO_2 sequestration plumes as they control the bubble or droplet dilution dynamics and lead to a chaotic, heterogeneous concentration field of the dissolved phase which can have significant environmental impacts. Several studies have measured turbulent quantities near (Soga and Rehmann 2004; Wain and Rehmann 2005; García and García 2006), statistics within (Simiano et al. 2006), and average mixing properties (Milgram 1983; McGinnis et al. 2004; Socolofsky and Adams 2005; Seol et al. 2007; Tekeli and Maxwell 1978) of bubble plumes, yet little is known regarding eddy characteristics and coherent structures in multiphase plumes. In this chapter, we present results of physical experiments of bubble plumes that identify vortices and quantify their

properties using the particle image velocimetry (PIV) method. These data are important to characterize the flow structures generating mixing and controlling the instantaneous dilution and concentration fields in multiphase plumes.

A detailed numerical model of a bubble plume is presented in Buscaglia et al. (2002), and identifies differences in entrainment and mass transfer when accounting for turbulence as compared to results generated using self-similar integral models. Though the model is an unsteady Reynolds average Navier-Stokes (URANS) simulation that does not capture coherent structures in the turbulence, the results underscore the importance of resolving turbulence-scale processes when mass transfer from the dispersed phase is considered. Non-linear interactions between the flow and concentration equations lead to transport rates not predicted by bulk integral models. Bombardelli et al. (2003) shows the predicted enhanced mixing of a bubble plume when using a Large Eddy Simulation (LES) over a $k - \varepsilon$ model, further enforcing the need to resolve turbulent structures.

Laboratory experiments further illustrate the importance of understanding turbulent structures responsible or plume wandering and entrainment in multiphase plumes. Bubble plume wandering is an aspect of mixing which results in a spreading of the mean velocity profile and is driven by low frequency plume turbulence. Plume wandering and enhanced tank mixing has been investigated using pressure sensors (Díaz et al. 2006; Buwa and Ranade 2002), acoustic Doppler velocimeters (ADV) (García and García 2006), laser doppler anemometry (LDA) (Mudde and Akker 1999; Becker et al. 1999), and various other techniques (Rensen and Roig 2001; Brenn et al. 2002). Soga

and Rehmann (2004) followed by Wain and Rehmann (2005) used ADV and temperature measurements outside the plume to calculate the dissipation and eddy diffusivity, respectively. García and García (2006) also used ADV data sampled at 10 and 25 Hz to establish a relationship between the buoyancy flux of the bubbles and the turbulent kinetic energy, integral length scale, and dissipation rates outside the bubble plume. Each of these studies focuses on the region outside the bubbly flow due to the ADV's inability to correctly process changes in phase. These studies provide important insight on turbulence structure outside bubble plumes, but do not investigate turbulence properties within the plume, where turbulent energy and coherent structures are generated. Laser Doppler Anemometry has been used to successfully measure turbulent properties within a bubble column (Mudde et al. 1997), but not a three dimensional bubble plume.

Most recently, PIV has become a noninvasive way to measure the mean and instantaneous flow fields in bubbly flows. PIV was used by Seol and Socolofsky (2007, 2008) to find mean flow characteristics and velocity intermittency, while Simiano et al. (2006) used PIV to measure average turbulent intensity profiles within a bubble plume and to investigate plume wandering. Simiano et al. also report the mean turbulent stresses, but did not quantify turbulent production or dissipation. While these data are important to understand turbulence, there remains a need to investigate vortical and coherent structures in bubble plumes.

To improve the understanding of turbulence in bubble plumes, this chapter applies PIV to identify individual vortices and to quantify several metrics describing

them throughout the bubbly flow region of the plume. We also present mean turbulent stresses and turbulent energy spectra to add insight to the turbulence properties and scales in bubble plumes. Section II details the experimental setup used to capture images for the PIV method. The image pre-processing to remove bubble signatures and the post-processing methods to identify vortices and compute quantitative metrics describing them are explained in Section III Data Analysis. The results are discussed in Section IV, including measures of vortex size, circulation, and enstrophy along with turbulent intensity profiles and energy spectra.

2.2 Experimental Methods

2.2.1 Experimental Setup

The experiments are performed in a large glass-walled experimental tank (1 m by 2 m in cross section by 1.5 m deep) in the Ocean Engineering Wave Tank Laboratory of the Zachry Department of Civil Engineering at Texas A&M University. The bubble plume is generated using an aquarium airstone diffuser with a diameter of 1.4 cm. A needle valve and air mass flow meter are used to regulate three different flow rates of 0.5, 1.0, and 1.5 l/min of bubbles at standard temperature and pressure. The combination of the diffuser and air flow rates provides a characteristic bubble diameter of 2.0 mm (Socolofsky 2001). The bubble size is verified visually by calculating the size of the bubbles from the raw images.

A plane of illumination is produced along the centerline of the bubble plume using light-sheet optics with an Argon-Ion continuous laser operating at 3 Watts. The

PIV seeding particles used are PSP polyamide particles with a mean diameter of 50 μm manufactured by Dantec Dynamics. To capture the illuminated seeding particles, a high speed Phantom camera is employed to image a 15 cm by 15 cm region at 250 Hz single frame rate with an exposure time of 10 μs. The camera has a resolution of 1024 pixels by 1024 pixels which results in each pixel representing 0.15 mm of the plume. The camera's field of view begins 30 cm above the diffuser with the plume centerline located 4.5 cm from the left edge of the image. The plume is placed asymmetrically in the field of view due to the oscillations of the bubble plume in the tank and to allow for comparisons in the dynamics of the plume from the plume center, throughout the entire range of the shear layer, into the quiescent ambient fluid. Images are stored during the experiments in the camera's 1 GB internal memory, which provides a maximum of four seconds of continuous data at 250 Hz. Since the data from four seconds is not adequate to achieve stationary turbulence statistics, the experiments are performed five times for a total of 20 s of data at each flow rate.

2.2.2 Bubble Plume Characteristics

The experiment is conducted at three different air flow rates that allow for comparisons to be made when the buoyancy flux is varied. Bubble plume properties are often correlated with the buoyancy flux and slip velocity, or terminal rise velocity in a quiescent fluid, of the dispersed phase (in this case, bubbles) (Socolofsky and Adams 2005). The slip velocity w_b of bubbles with a characteristic diameter of 2 mm is 20 cm/s (Clift et al. 1978). Bombardelli et al. (2007) combine these parameters to establish a characteristic length scale in the plume D given as

$$D = \frac{gQ_g}{4\pi\alpha^2 w_b^3} \qquad (2.1)$$

where g is the gravitational constant, Q_g is the volumetric air flow rate at the diffuser, and α is the entrainment coefficient, taken as 0.083; for air with a density of 1.2 g/cm^3 and making the Boussinesq approximation, the buoyancy flux of bubbles is gQ_g. Using this formulation, D in our experiments is equal to 11.8, 23.6, and 35.4 cm for Q_g of 0.5, 1.0, and 1.5 l/min, respectively. Thus the field of view for the experiments is at or above D. Bombardelli et al. show that the plume flow properties become asymptotic (independent of initial conditions) when $z/D > 1$; hence, the measurements presented below are for the asymptotic region of the bubble plume flow.

The experimental results are made nondimensional by use of the plume radius along with gQ_g and w_b. For this study the plume radius r is calculated as the point at which the time-averaged vertical velocity v divided by the centerline velocity (maximum time-average velocity in a cross-section) v_c is equal to the quantity $1/e$.

To evaluate the camera resolution, we also require an estimate of the Kolmogorov length scale given as

$$\eta = \left(\frac{v^3}{\varepsilon}\right)^{1/4} \qquad (2.2)$$

where v is the kinematic viscosity and ε is the dissipation (Mathieu and Scott 2000). The viscosity of water is commonly known to be 9.55×10^{-7} m^2/s at the experimental

room temperature of 22 degrees Celsius and the average dissipation can be taken from experiments performed by Soga and Rehmann (2004) as $\varepsilon = 4 \times 10^{-8}$ m^2/s^3. Using these quantities, η is calculated to be approximately 2 mm. This is on the same order as the diameter of the bubbles and, thus also, the predicted vortex production size in the bubble wakes. Although η is a rough estimate of the smallest eddy size, this suggests that either the turbulent energy in the bubble wake eddies is dissipated by viscosity without need of energy cascade to smaller scales or that the dissipation rate taken from Soga and Rehmann from outside the bubble plume cannot be applied inside the bubble plume to estimate the order of η. In either case, the camera resolution of 0.15 mm/pixel is well below the expected Kolmogorov scale threshold.

2.3 Data Analysis

2.3.1 Image Pre-Processing and PIV Analysis

Because the images captured in the experiments contain both bubbles and PIV tracer particles, the bubble signatures must be removed from the images before PIV can be applied to measure the continuous phase velocity field. Alternatively, bubble images could have been removed using optical filters and fluorescent PIV tracer particles; Seol and Socolofsky (2008) show that the procedure applied here is equally accurate. Figure 2.1 displays a portion of an image taken during the experiments (sub-figure a) and the post-processed result after removing the bubbles (sub-figure b). In the raw images, most of the bubbles are larger (about 75 pixels in area) and darker than the PIV tracer particles (about 5 pixels in diameter); however, some bubbles directly in the laser light sheet are

brighter than the PIV tracer particles. In order to remove all of the bubbles, bubbles are identified using two different criteria, the first of which eliminates bubbles based on their brightness, and the second of which eliminates bubbles based on their size, similarly to Khalitov and Longmire (2002).

a)

b)
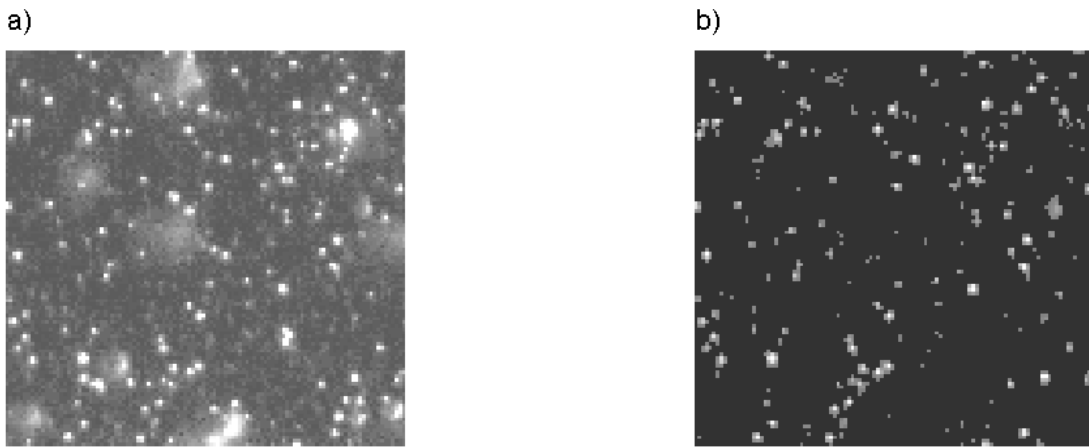
Fig. 2.1. Portion of a raw image before (a) and after (b) being processed for bubble removal.

First, the image is transformed to black and white using a constant intensity threshold via the Matlab® function **im2bw**. This eliminates dimly lit bubbles and tracer particles that are outside the laser light sheet but illuminated from reflected light. The final cut-off intensity threshold was found by adjusting the value and visually inspecting the filtered results to confirm that tracer particles in the light sheet are not removed while dimly lit bubbles were removed. Second, the area open algorithm is applied to the black and white image to remove contiguous objects below a cut-off size, which is accomplished with the Matlab® function **bwareaopen**. The resulting bubble image is

subtracted from the previous black and white image, resulting in a particle image that contains only particles. This image is multiplied by the original gray-scale image to obtain a gray-scale image containing particles only. Finally, the areas removed from the gray-scale image are replaced by the mean background intensity so that their dark regions do not bias the PIV results. As seen in Figure 2.1, the bubbles are successfully removed while the particles in the light sheet remain with their original light intensity pattern.

The PIV analysis is performed in DaVis (LaVision GmbH 2002) using a multi-pass algorithm and images already corrected for geometric distortion. The program applies the regular cross-correlation PIV algorithm with 50% overlap for a 32 by 32 pixel interrogation window followed by a second pass with an interrogation widow size of 16 by 16 pixel. This provides velocity data on an 8 by 8 pixel grid, which results in velocity vectors every 1.2 mm over the entire field of view—approximately at the Kolmogorov length scale. Since the bubbles have a diameter of 2 mm, vortices shed in the bubble wakes are just below the resolution of the PIV velocity data. Finally, error vectors are removed using the vector median filter which compares the value of a vector with the root mean square of the neighboring vectors.

Regions where bubbles or error vectors were removed result in gaps in the PIV vector maps. The bubble diameters for the experiments ranged from 10 to 22 pixels, while the bubbles move 10 to 12 pixels between images, resulting in every bubble removing about one and a half times its size worth of data for every vector map. As an example, for the 0.5 l/min case, the average void fraction across the plume is measured

as 2.5% from the raw PIV images. Estimating that vectors will be missing at a rate of one and a half times the average void fraction, it can be predicted that 3.75% of the vectors will be missing. The actual percentage of vectors that required filling averaged 5%. Thus, around 1% of vectors are removed due to PIV errors and 4% due to the presence of the dispersed phase.

The missing vector data are replaced using a Kriging interpolation method. Filling in the missing data is necessary so that velocity gradients and other flow properties can be computed as continuous functions throughout the flow field using finite-difference methods. This would have been the natural result had fluorescent particles and optical filters been employed to capture the raw PIV images. Because a very low number of vectors are added, the interpolation is not expected to bias the results, and none of the measured velocity data are replaced by interpolation. The Kriging interpolation method used is from the Matlab® toolbox **DACE** (Lophaven et al. 2002). The Kriging method selected uses an exponential correlation function and a first-order polynomial regression model to fill in missing data, resulting in a complete, continuous velocity vector map for the continuous phase.

2.3.2 Vortex Identification Method

Once the PIV calculations and vector post-processing is complete, the continuous phase vector maps are interrogated to identify the vortical and coherent structures in the flow field. Figure 2.2 shows a sample of a completed instantaneous vector map. The plume centerline is at zero on the x-axis, and the plume edge is at about 50 mm (plume radius for this flow rate of bubbles is 38 mm). By its nature, the PIV data are a planar slice

through the centerline of the plume. Because the vortices are three-dimensional, some of the vortex signatures in the PIV data will be off-center slices through spherical and other-shaped vortices, and the vortex cross-sections will not exactly represent the maximum size of all the identified vortices. This data is nonetheless important since it can be easily compared to data from three-dimensional numerical models and because it still leads to important insight on the characteristics of vortices and their distribution along the plume cross-section and in the ambient flow.

Many methods can be applied to identify vortical structures two-dimensional PIV data, but for a shear flow such as depicted in Figure 2.2, the local swirl strength criterion has been shown by Adrian et al. (2000) to be the most effective at identifying the full range of vortices, independent of their instantaneous convection velocity. The local swirl strength can be found by constructing an equivalent two-dimensional velocity gradient tensor $d^{2\text{-}D}$ given by

$$d^{2-D} = \begin{bmatrix} \dfrac{\partial u}{\partial x} & \dfrac{\partial u}{\partial y} \\ \dfrac{\partial v}{\partial x} & \dfrac{\partial v}{\partial y} \end{bmatrix} \tag{2.3}$$

where u and v are the instantaneous velocity vectors in the lateral x and vertical y coordinate directions, respectively. The velocity gradients are calculated from the PIV data using a four-point centered least squares method (Raffel et al, 1998). The swirl strength is the imaginary part of the complex conjugate eigenvalues of the stress tensor $d^{2\text{-}D}$, and represents the local frequency of rotation, independent of the velocity shear.

Thus, all locations of non-zero swirl strength contain vortical motion, and Adrian et al.

showed that vortices are identified as contiguous regions of non-zero swirl strength.
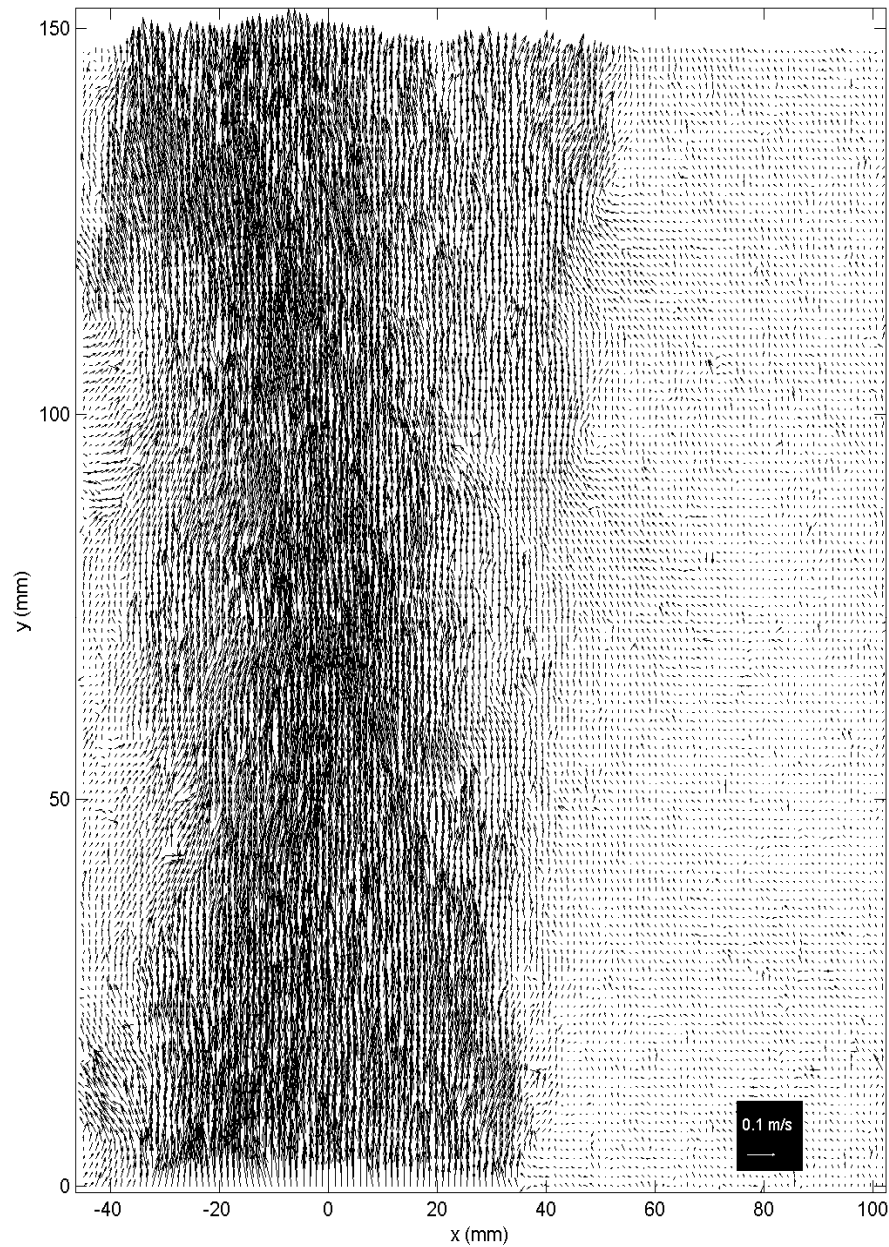
Fig. 2.2.   Instantaneous velocity field in a bubble plume for the 0.5 l/min case.

Figure 2.3 shows a small portion of a velocity field for the 0.5 l/min case in which the instantaneous velocity field (subplot a) shows little evidence of a vortex. However the local swirl strength identifies a vortex which is clearly visible in the data after subtracting the convective velocity given by the velocity at the point of highest local swirl strength. Using this method, vortices in the continuous phase are identified for the entire velocity field. In order to apply a Nyquist-type minimum resolution criteria to the data, only vortices with two or more points of adjacent non-zero swirl strength are considered in the remaining analysis.
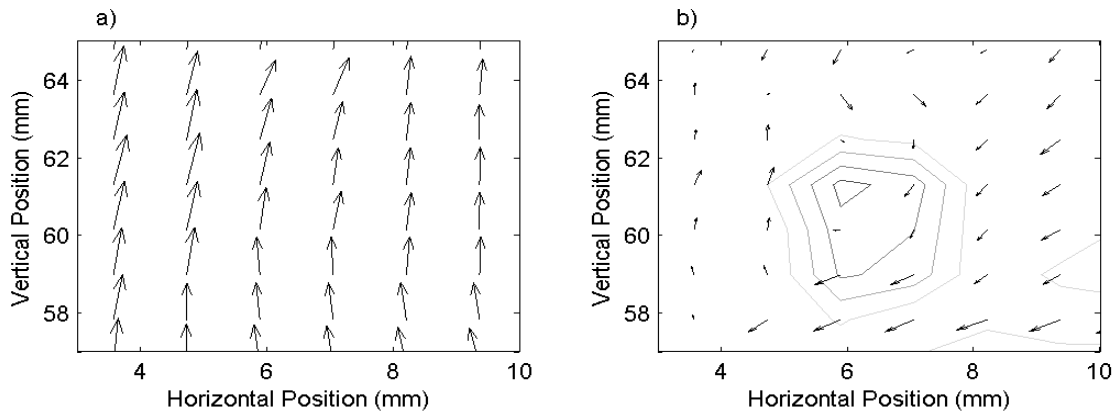
Fig. 2.3. Example of the location of a vortex by using the local swirl strength: the instantaneous flow field (a) and the velocity field with the convection velocity at the peak of the swirl strength removed along with contours of the swirl strength (b).

Figure 2.4 shows the identified vortex map with contours of swirl strength for the velocity vector map depicted in Figure 2.2. It is clear in the figure that the majority of vortices are identified in the bubble plume, and that these vortices have larger swirl

strength and are, thus, more energetic than those outside the plume. Some of the largest vortices are present in the shear layer near the edge of the plume, and these attributes are quantified in more detail in the results section to follow.
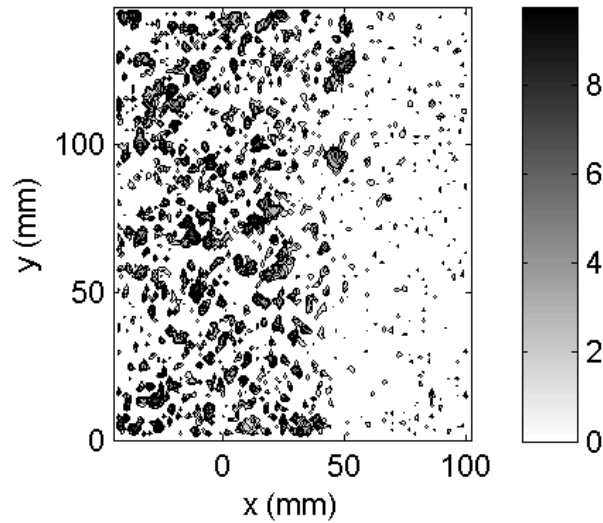
Fig. 2.4. Instantaneous map of identified vortices showing contours of swirl strength.

2.3.3 Metrics Quantifying Vortex Properties

Metrics describing the identified vortices are computed using the velocity vector and vorticity fields. The vorticity is computed from its velocity gradient definition using the four-point velocity gradient estimate used to compute $d^{2\text{-}D}$. Figure 2.5 shows the instantaneous vorticity field for the velocity vector map of Figure 2.2. Higher vorticity is present in the plume and plume shear layers between ±50 mm; because of the high shear, individual vortices are difficult to identify using vorticity alone, hence, the need to use local swirl strength to identify vortices.

To quantify the properties of individual vortices, a clipping procedure is required. Using the Matlab® imaging toolbox, the map of local swirl strength is converted to black and white with white representing any non-zero local swirl strength value, and the function **bwlabel** is used to assign a number to each vortex in the flow field. Each identified vortex is then easily indexed, its position identified, and used to clip the velocity and vorticity maps, resulting in fields for the identified vortex only. Metrics for
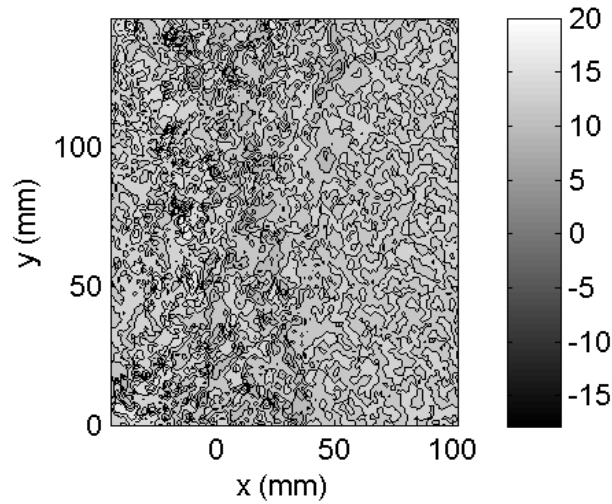
Fig. 2.5. Instantaneous vorticity field.

each vortex are then computed, including the vortex size (surface area in the two-dimensional PIV slice through the plume), circulation (computed as the sum of the vorticity over the area of the vortex), and enstrophy (computed as the sum of the square of the vorticity over the area of the vortex). The circulation and enstrophy are found by

summing the vorticity and vorticity squared values for each cell of the identified vortex and multiplying the result by the area contained in a cell.

Figures 2.6 and 2.7 illustrates these calculations for the instantaneous vector map in Figure 2.2. Figure 2.6 shows the probability density function (PDF) of vortex size (subplot a) and the average vortex size as a function of position in the plume (subplot b). The PDF is computed using all of the vortices identified throughout the field of view for the single, instantaneous PIV vector map. To compute the average vortex size as a function of position, the lateral dimension is segmented into bins, and the average size of all vortices identified in each bin is plotted at the center of each bin. Although the plume is spreading out slightly with height, the field of view is small enough that the bin sizes used are not affected by the plume spread. From Figure 2.6(b), the larger vortices are present in the plume (the plume edge is identified by the dotted lines) with smaller vortices in the ambient fluid, and several images will be required to achieve stationary statistics for each bin.

The average vortex circulation (subplot a) and enstrophy (subplot b) as a function of lateral position is illustrated in Figure 2.7 for the instantaneous PIV vector map in Figure 2.2. Again, averages versus lateral position are computed using bins, and a single image does not provide stationary statistics for the average. However, the trend for larger circulation and enstrophy within the plume is clear.
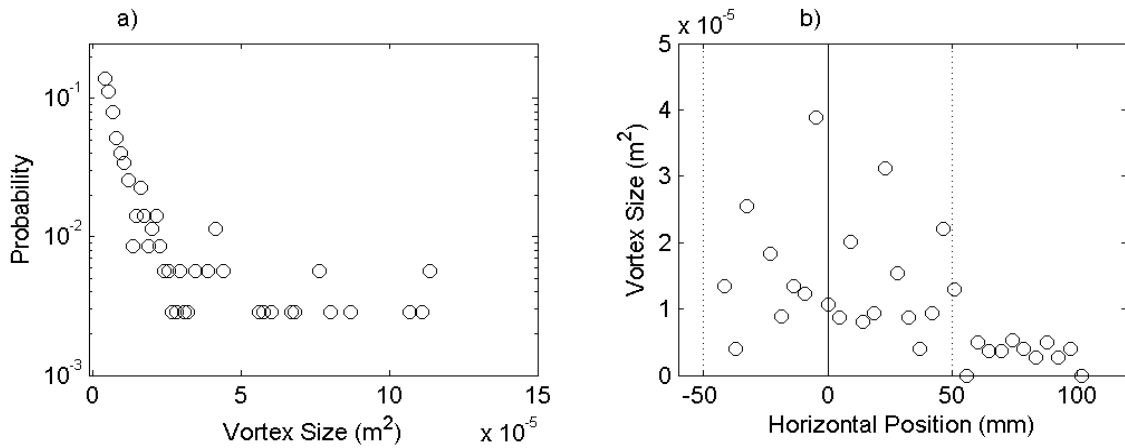
Fig. 2.6. Example of a vortex size probability distribution (a) and average vortex size versus plume position (b) for a single velocity field with the solid line representing the plume center and the dotted line marking the plume edge in subplot (b).
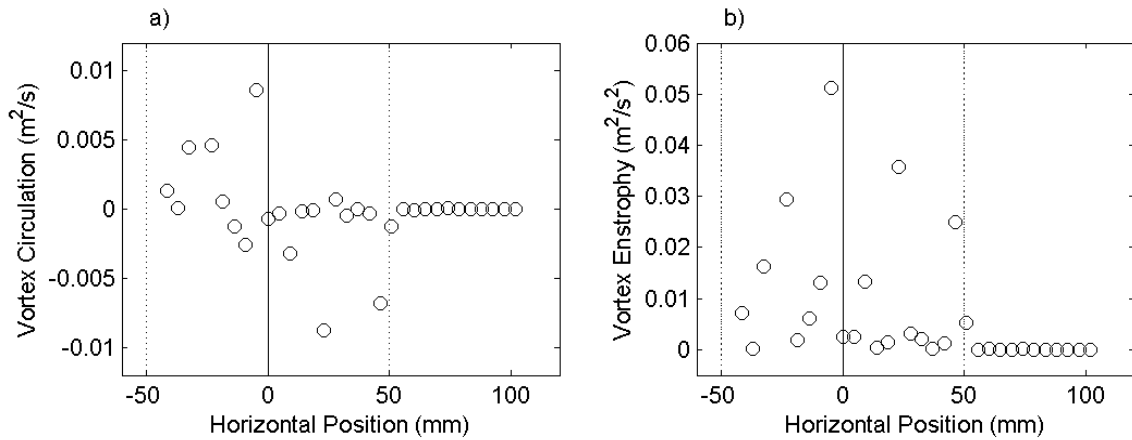
Fig. 2.7. Example of the vortex circulation (a) and enstrophy (b) versus position in the plume for a single velocity field with the solid line representing the plume centerline and the dotted line marking the plume edge.

2.4 Results

2.4.1 Time-Averaged Properties of the Flow Field

Using the velocity fields computed from the PIV analysis, instantaneous and mean properties of the continuous phase are calculated, including the identification of individual vortices and quantification of the turbulence properties. Figure 2.8 depicts mean profiles of the velocity components u and v.   The velocity profiles are nondimensionalized by the time-average centerline velocity v_c and the plume radius r. Using this formulation, self-similarity is observed for the range of bubble buoyancy fluxes used in the experiments.   The v-component of the velocity fits a Gaussian distribution; the positive mean flow outside the plume represents the weak secondary currents present in the experimental tank.
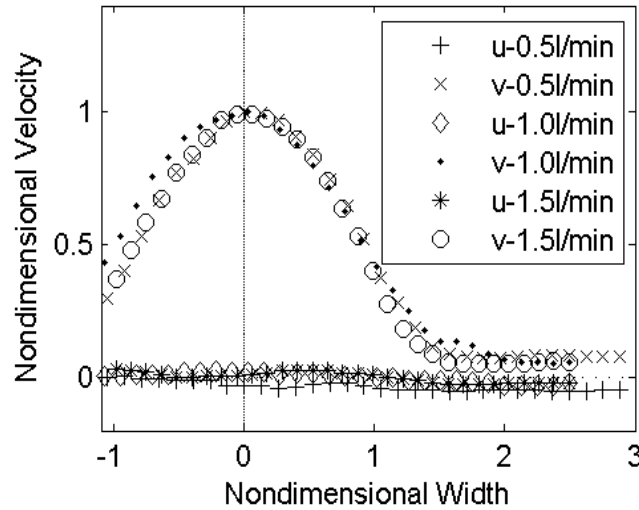
Fig. 2.8.   Average nondimensional velocity profile for the three experimental flow rates of 0.5, 1.0, and 1.5 l/min.

The time average vorticity and swirl strength are computed as the average of the instantaneous fields of vorticity and swirl strength, not from the time-average velocity, which would yield zero swirl strength. Figure 2.9 shows a contour map of the time-average vorticity for the 0.5 l/min case. The largest magnitude of the vorticity lies between 30 mm and 40 mm from the plume center and identifies the shear layer that exists between the plume central region and the ambient fluid. The average vorticity at the plume centerline is zero as expected.

Figure 2.10 depicts the time-averaged local swirl strength field for the 0.5 l/min experiment. The short, stripe-like patterns in the plume region represent vortices that persist over a long time in the experiments. The plume edge at ±50 mm is clearly identified in the figure, emphasizing that vortices in the ambient fluid are short-lived, less dense and have low swirl strength compared to vortices in the plume.
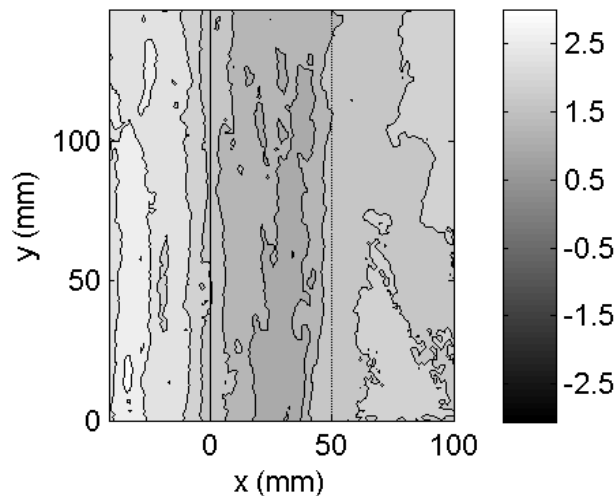
Fig. 2.9.   Average vorticity field for the 0.5 l/min experiments with a solid line representing the plume centerline and a dotted line marking the plume edge.
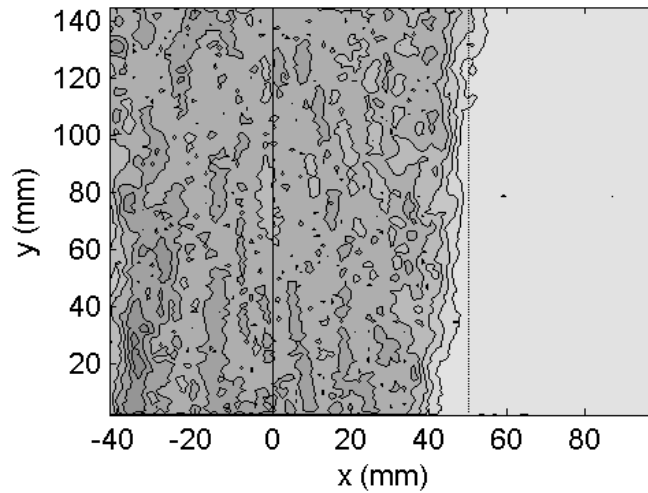
Fig. 2.10. Average local swirl strength field for the 0.5 l/min experiments with a solid line representing the plume centerline and a dotted line marking the plume edge.

Comparing Figures 2.9 and 2.10 shows that the plume edge (at ±50 mm) lies on average 10 mm from the maximum time-average vorticity (at ±40 mm), which corresponds roughly with the plume radius (which is 38 mm for the 0.5 l/min case depicted in the figures). This region represents the high-shear entrainment region of the plume and lies outside the core bubbly flow region, which extends to about 80% of the plume radius (or 30 mm) (Socolofsky and Adams 2005). From these data we can expect that eddies forming in the plume shear layer will grow to up to 10 mm in diameter, given by the difference between the locations of the shear layer and the plume edge. This corresponds to about one quarter of the plume radius r. Larger eddies are not expected due to the presence of the bubble column. Within the bubbly flow region, Shawkat et al. (2007) show for pipe flow that the effect of the bubbles is to reduce the characteristic

length scale from the pipe radius to the average distance between bubbles. Thus, we can also anticipate that smaller characteristic vortices will be present in the bubble plume core.

2.4.2 Characteristics of Identified Vortices

The probability of the nondimensional vortex size for each bubble flow rate (subplot a) is shown in Figure 2.11 along with the time-averaged nondimensional vortex size versus position in the plume (subplot b). The vortex size (vortex surface area in the PIV cross-section) is nondimensionalized by the plume radius squared. Using this nondimensionalization, each of the flow rates investigated collapse to a single PDF for vortex size (subplot a). Subplot (b) in Figure 2.11 also confirms the expected distribution of vortex sizes in the plume: the vortex size is greatest in the plume shear layer at $x/r = 1$, and is reduced along the plume centerline. Figure 2.12 shows the lateral distribution of the largest vortices identified in the plume versus lateral position. Here the largest vortices are also in the plume shear layer. For each of the three flow rates, the largest vortices have effective radii of 10.0, 10.3, and 12.0 mm for the experimental bubble flow rates of 0.5, 1.0, and 1.5 l/min. Each of these experiments also had plume widths of 37.7, 38.7, and 42.7 mm, respectively. This confirms that the largest vortices in the plume are about one quarter of the plume width. Thus, it is concluded that the largest vortices are a product of the instabilities in the plume shear layer which is related to the average shear velocity profile, and that vortex size in the center of the plume is reduced due to the presence of the bubbles. The presence of vortices within the middle of the plume can be attributed to both diffusion from the plume shear layers and bubble

wake interaction, but it is difficult to estimate the contribution from each mechanism. Vortices in the ambient fluid are on average half the size of vortices in the plume. The profiles also show good agreement in nondimensional space across all flow rates. To understand the mixing and energy potential of the identified vortices, their circulation and enstrophy versus lateral position are shown in Figure 2.13. Subplot (a) depicts the average circulation of each vortex versus position in the plume, and subplot (b) the average enstrophy. Circulation is nondimensionalized by the time average centerline velocity v_c and plume radius r and the enstrophy by v_c^2 and r. As with the vorticity, the magnitude of the circulation is maximum in the plume shear layer. This is due to the higher vorticity combined with the presence of larger vortices. Because the average circulation changes sign from one side to the other of the plume, the plume centerline necessarily predicts vortices with zero circulation on average. These vortices are not without energy, however. The enstrophy distribution (subplot b) clarifies this fact. The enstrophy is also maximum in the shear layers; hence, vortices in the shear layers are the most energetic, followed by vortices in the plume center. Vortices in the ambient fluid outside the plume have very low enstrophy and thus low energy. The nondimensional profiles of vortex circulation and enstrophy also show good agreement across flow rates, with the greatest difference for the enstrophy in the plume shear layers ($x/r = \pm 1$).
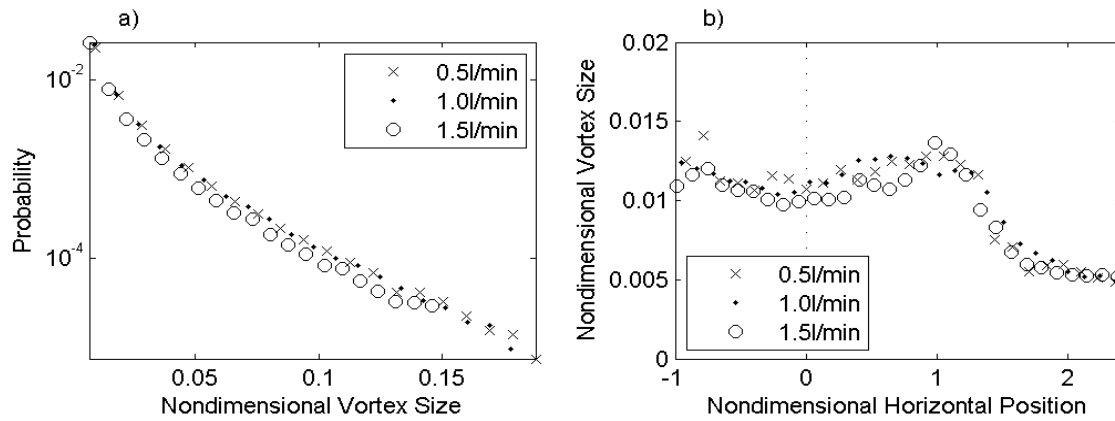
Fig. 2.11. Average probability distribution function for nondimensionalized vortex size (a) and average vortex size versus position in the plume (b) for all experimental flow rates.
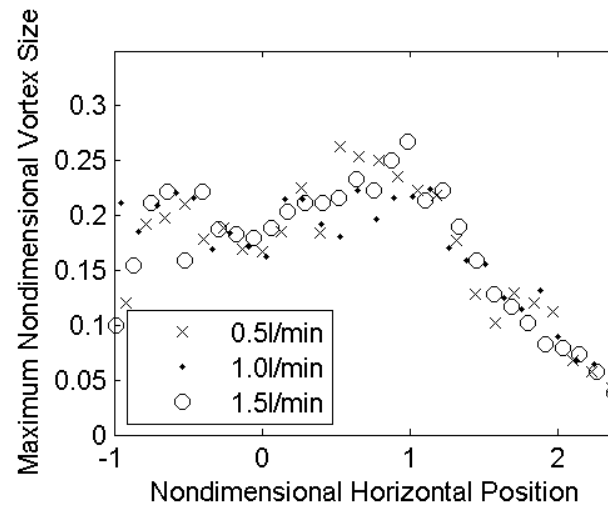
Fig. 2.12. Nondimensionalized vortex size for the largest vortices identified in each region versus position in the plume for all experimental flow rates.
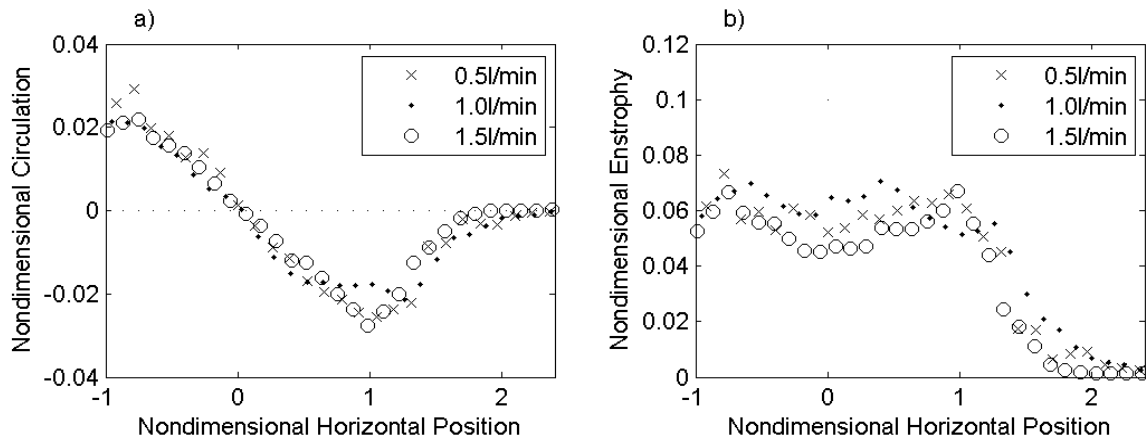
Fig. 2.13. Average nondimensional circulation (a) and enstrophy (b) versus plume position for all experimental flow rates.

Figure 2.14 combines the results of Figure 2.11 and 2.13 to give the correlation of the magnitude of the vortex circulation (subplot a) and enstrophy (subplot b) with vortex size. The figure clearly shows that the vortex size is the major factor determining the expected circulation or enstrophy of each identified vortex throughout the plume and into the quiescent ambient fluid. These results are also confirmed across all flow rates and collapse well in nondimensional space.

To check the convergence of these turbulent results, a comparison was made with time-averages of 12 seconds of data (3000 velocity fields) and the full data set of 20 seconds (5000 velocity fields). Figure 2.15 shows this comparison for an airflow rate of 0.5 l/min for the nondimensional vortex size (subplot a) and nondimensional circulation (subplot b) versus the nondimensional horizontal position. The convergence was also checked for the average vorticity contours, average swirl strength contours, PDF of the

vortex size and average enstrophy, ensuring these turbulent metrics represented the time-averaged results accurately.
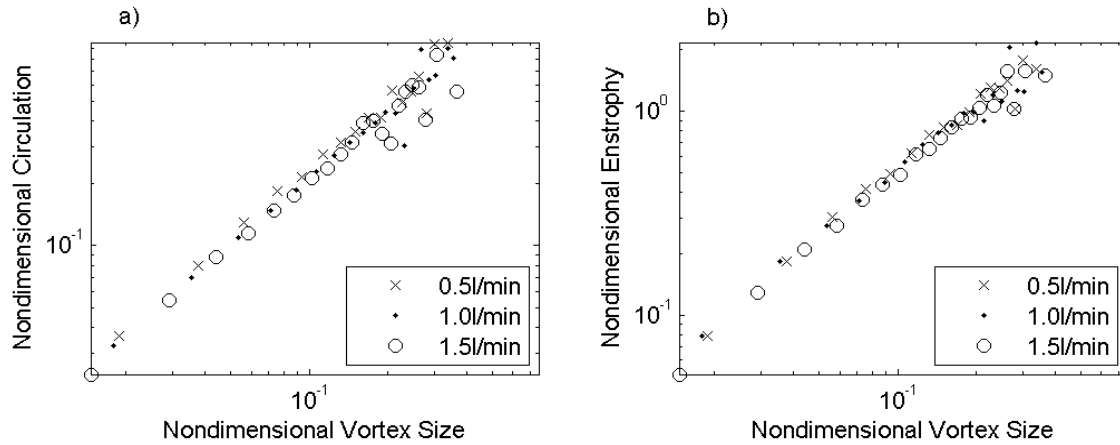
Fig. 2.14. Comparison of nondimensional vortex size versus nondimensional circulation (a) and enstrophy (b).
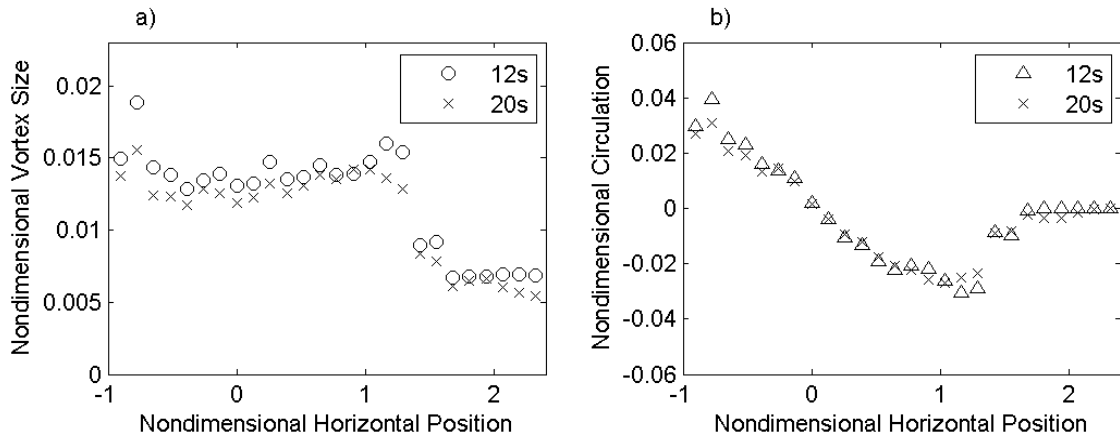
Fig. 2.15. Comparison of the nondimensional vortex size (a) and nondimensional circulation (b) for 12 and 20 seconds worth of data versus the nondimensional horizontal position for an airflow rate of 0.5 l/min.

2.4.3 Turbulence Statistics

To provide more typical turbulence measures from these experiments, we also present results for turbulent stresses and energy spectra. Following in the example of Simiano et al. (2006), the average turbulent stresses are given in Figure 2.16. Unlike Simiano et al., who nondimensionalized the average turbulent stresses by the local void fraction χ times the bubble velocity squared, the average turbulent stresses with respect to the plume position are presented here nondimensionalized by the local time-average velocity $v(x)$ shown in Figure 2.8. The formulation given here is preferred since the void fraction is already non-dimensional, making it unclear how to appropriately include the void fraction in the parameterization.   It appears that the important effect is that the independent variable, either χ or v, should have a Gaussian profile to achieve a collapse of the data.   If the turbulent stresses are a result of bubble wakes, χ may be more appropriate; whereas, if the turbulent stresses are due to instability of the mean velocity, v may be more appropriate. The data presented here indicate that instability in the plume shear layer is the dominant mechanism for generation of large-scale vortices.   The Reynolds stresses presented in Simiano et al. show similar trends to those in Figure 2.16; however, direct comparison is not possible since the void fraction profiles needed to convert their data to the current formulation are not available. In either case, the data are cut off at the edge of the plume, where the void fraction or average plume velocity tends to zero. The stresses are fairly uniform in the bubbly region of the plume, and increase in the plume shear layer near ± 1.
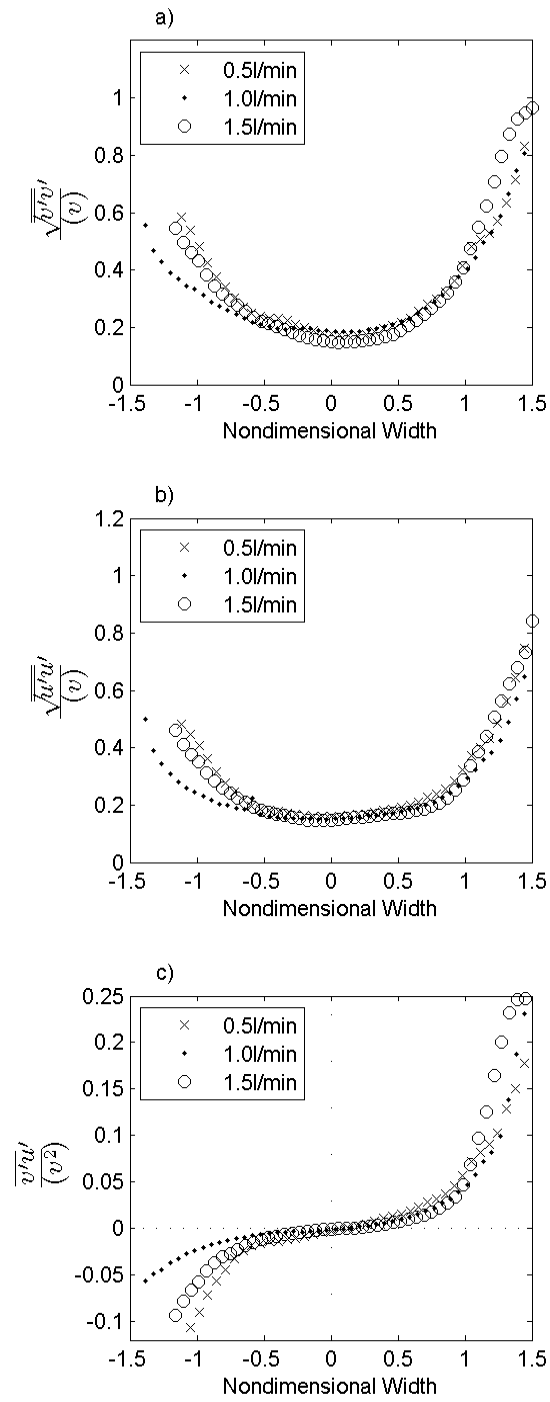
Fig. 2.16. Average nondimensional turbulent stresses versus position in the plume for all experimental flow rates.

Autocorrelation functions and turbulent energy spectra are presented in Figure 2.17 for three locations along the plume axis: the plume centerline (subplots a and d), the midpoint between the plume centerline and the plume edge (subplots b and e), and the plume edge (subplots c and f). Column 1 in the figure gives the autocorrelation of the fluctuations of the vertical velocity component v'. As shown by Shawak et al. (2007) for bubbly pipe flow, the presence of bubbles changes the curvature of the autocorrelation function at zero lag compared with a non-bubbly flow, which corresponds to a decrease in the dissipation length scale. The results in Figure 2.17 for the plume center compared to the plume edge illustrate similar results for the bubble plume flow.

Integrating these autocorrelation functions up to the point at which the correlation value becomes negative leads to a characteristic time scale which can be converted to a characteristic length scale L_1 by multiplying by the local time-averaged velocity. This characteristic length scale L_1 is used to nondimensionalize the energy spectra in Figure 2.16, as was done by Shawak et al. Table 2.1 presents L_1 for each buoyancy flux of bubbles investigated and at each of the three positions in the plume presented in Figure 2.17. From the table, it is seen that the nondimensional length scale fluctuates somewhat, but is independent of location and approximately equal to one quarter of the plume radius. This is in agreement with our previous estimate of the large-scale vortices based on their formation in the plume shear layer and their limited scale due to destruction of larger-scale vortices by the bubble. Hence, the largest, most
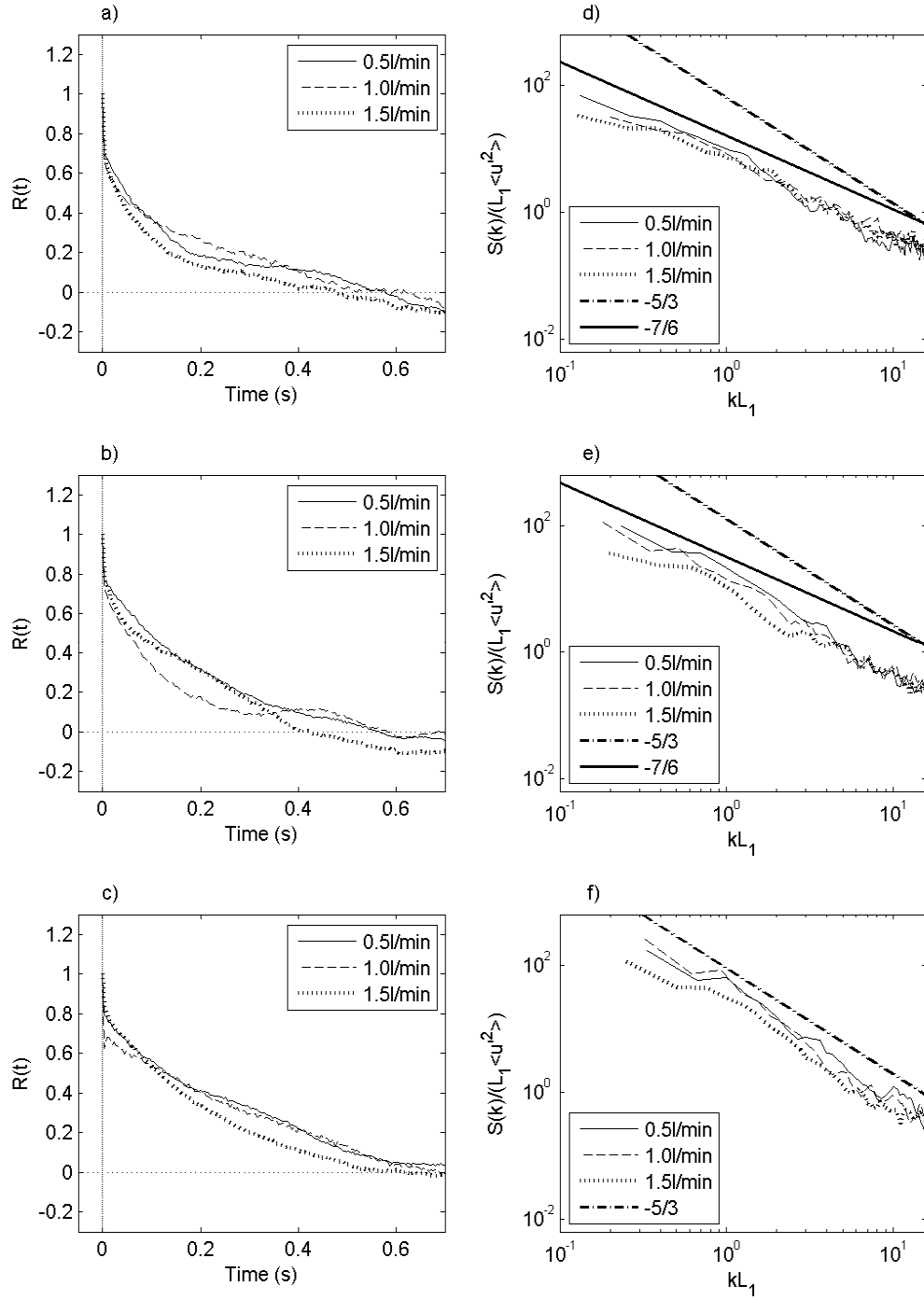
Fig. 2.17. Autocorrelation function of the turbulence and nondimensionalized turbulent energy spectrum for three positions in the plume: (a and d) plume center, (b and e) midpoint between plume center and plume edge, and (c and f) plume edge for all experimental flow rates.

energetic vortices are generated in the plume shear layer and scale as about one quarter of the plume radius.

Table 2.1.   Characteristic length scale L_1 for each flow rate reported at the plume center (a), midpoint between the plume center and edge (b), and at the plume edge (c).

Buoyancy Flux (l/min)	L_1/r		
	(a) Plume Center	(b) Midpoint Between Center and Edge	(c) Plume Edge
0.5	0.28	0.301	0.22
1.0	0.39	0.25	0.20
1.5	0.30	0.40	0.24

The energy spectra in Figure 2.17 are the average of the energy spectra for each four-second span of images from the experiments. The data are nondimensionalized by the characteristic length scale and the Reynolds stresses $\overline{v'^2}$.   With this nondimensionalization, the data collapse well for all three bubble buoyancy fluxes investigated. Along with the energy spectra, the classic dissipation rate of -5/3 is also plotted. The dissipation rate in the center of the plume is less than the -5/3 law due to the production of turbulence from the bubbles at smaller scales and reduction of energy at larger scale, similar to that found by Shawak et al. (2007) and Rensen et al. (2005) in two-phase pipe flow. Lance and Bataille (1991) also reported a change in the turbulent energy spectra with exponents of -1 at low frequencies and -8/3 at high frequencies.

Bolotnov et al. (2008) compared the results of Rensen et al. and Lance and Bataille concluding that the slope for the inertial subrange to be ~ -7/6 and a slope between -8/3 and -11/3 for the dissipation range. This study does not resolve the dissipation range but found good agreement with a slope of -7/6 for the inertial subrange along the plume centerline. At the mid-point between the center and plume edge the slope is much closer to -5/3 but appears to be slightly less. At the plume edge, the dissipation rate is very close to -5/3. Hence, the bubble core modulates the turbulent energy spectra only in the regions where there are bubbles, and otherwise the flow behaves similarly to a single-phase flow, with vortex generation in the plume shear layer and dissipation rates matching the -5/3 single-phase rate.

2.5 Summary and Conclusions

PIV was used to develop two-dimensional velocity fields within and near a bubble plume for flow rates of 0.5, 1.0, and 1.5 standard l/min in the laboratory. The images were processed prior to PIV to remove bubble signatures, allowing for the direct measurement of the velocity field of the continuous phase. Once the PIV data were computed, a median filter was used to eliminate error vectors, and a Kriging interpolation algorithm was used to fill in missing vectors due to removal of the bubbles and the elimination of error vectors. From the resulting continuous velocity fields, the local vorticity and swirl strength were computed using a four-point least-squares finite difference method. Individual vortices were identified for contiguous regions of non-zero swirl strength, and vortex properties, including size, circulation, and enstrophy were calculated across all experimental images and as a function of position in the plume.

Turbulent statistics, including turbulent stresses, characteristics length scales, and energy spectra were also presented.

All of the quantitative metrics describing the identified vortices in the plume scale well with the time-average centerline velocity v_c and the characteristic plume radius r. No further dependence on the bubble characteristics, void fraction, or buoyancy flux was necessary to achieve a collapse of the data. The vortex characteristics further show a direct relationship between vortex size and vortex energy (measured both by the magnitude of the circulation and the enstrophy), with the largest vortices present in the plume shear layer at a radial distance equal to the characteristic plume radius r and with a characteristic size of one quarter of r.

The combined velocity field and vortex characteristics data indicate that the largest and most energetic vortices are generated by shear instability of the continuous phase fluid within the plume shear layer. This region has relatively few bubbles, and exhibits typical properties of single-phase plumes. The bubbly flow in the plume center breaks up the larger vortices generated at the plume edge, resulting in smaller average sizes of vortices and provides turbulence production on a smaller length scale comparable to the bubble separation distance.

Further analysis of the turbulence energy spectra confirms the results of the vortex characteristics analysis. The dissipation rate is reduced on the plume centerline due to fine-scale turbulence production by the bubbles, but conforms to the -5/3 dissipation law outside the bubble column, in the plume shear layer and at the edge of the plume. Hence, two-phase plumes exhibit two-phase behavior modulated by the

bubbles within the bubble core, and single-phase behavior in the plume shear layers and outside the plume, where relatively few bubbles are present. The generation of large-scale vortices at the plume edge and subsequent modulation in the bubble plume core work together to control the vortex dynamics in bubble plumes, and affect the mixing characteristics of multiphase plumes.

CHAPTER III

MEAN AND TURBULENT PROPERTIES OF INERTIAL

PARTICLE PLUMES

High-speed PIV experiments were conducted to quantify the mean and turbulent properties of inertial particle plumes. Three different mass fluxes were used in combination with three different particles sizes, each with a specific gravity of 2.5, giving a total of 9 cases. The raw images were preprocessed to remove the dispersed phase (inertial particles), leaving only the continuous phase for PIV analysis. The resulting velocity fields were used to calculate the vorticity and local swirl strength whose coupling provided the quantification of vortices in the flow. The results show the time-averaged velocity fields and vorticity field to be self-similar for all the particle test cases. The average vortex properties of the flow were self-similar for two larger particle sizes whereas the smallest particle size more closely matched that of the bubble plume data. Analysis of the velocity fields showed the time-averaged turbulent Reynolds stresses to be self-similar in the plume for the test cases. The vertical turbulent stress component, $v'v'$, was larger in the inertial particle plume than the bubble plume data. This chapter also presents results showing the modulation of the turbulent energy spectra from -5/3 to -7/6 due to the dispersed phase.

3.1 Introduction

Multiphase jets and plumes are common in both environmental and industrial applications including, bubble plumes, droplet plumes, and loop reactors. One subset of multiphase plumes occurring in the environment are negatively buoyant dispersed phase plumes such as sediment plumes and CO_2 sequestration plumes (Wannamaker and Adams 2006).

The mean and turbulent properties of multiphase plumes are difficult to measure experimentally since the dispersed phase interferes with measurement methods such as acoustic Doppler velocimetry (ADV) and laser Doppler velocimetry (LDV). Experiments conducted by Bryant et al. (2009) and Simiano et al. (2006) successfully used particle image velocimetry (PIV) to capture the turbulent stresses of bubble plumes. Furthermore, Bryant et al. (2009) analyzed the PIV data using vortex identification methods and found the largest, most energetic vortices lay along the plume edge in bubble plumes. However, the mean turbulent properties of inertial particle plumes have not been investigated using high-speed PIV.

Beyond turbulent stresses and vortex properties, investigation into the turbulent energy spectra of multiphase plumes are important with previous studies in bubbly pipe flow, finding the turbulent kinetic energy dissipation rate changing from the classical slope of -5/3 to -7/6 (Lance and Bataille 1991; Shawkat et al. 2007; Rensen et al. 2005). High-speed PIV has been used successfully by Bryant et al. (2009) to identify changes in the turbulent energy spectra due to the dispersed phase in bubble plumes.

This chapter presents a high-speed PIV study of an inertial particle plume quantifying the mean flow, turbulent Reynolds stresses, vortex properties, and turbulent energy spectra. The following section will detail the experimental setup, followed by sections explaining the analysis and results of this study.

3.2 Physical Model

The PIV experiments in this study were performed in a glass-walled tank measuring 1.0 m by 2.0 m by 1.5 m deep in the Ocean Engineering Wave Tank Laboratory of the Zachry Department of Civil Engineering at Texas A&M University. The plume was generated with particles having an average diameter of 2, 1.45, and 1.0 mm with a specific gravity of 2.5 and slip velocities, w_b, of 17.5, 12.6, and 8.0 cm/s, respectively. The slip velocities were calculated by performing PIV analysis of the inertial particles. Table 3.1 below details the nine test cases.

Table 3.1.   Mass flow rate and inertial particle diameter details for all test cases.

Case	Mass Flow Rate (kg/s)	Particle Diameter (mm)
A	0.0305	2.0
B	0.0265	2.0
C	0.0115	2.0
D	0.0168	1.45
E	0.0049	1.45
F	0.0030	1.45
G	0.0208	1.0
H	0.0071	1.0
I	0.0045	1.0

The particles were delivered through a funnel system at the water surface to minimize any initial velocity. The characteristic length to the asymptotic region of the plume from the diffuser is given by Bombardelli et al. 2007 as

$$D = \frac{gQ_g}{4\pi\alpha^2 w_b^3}$$

(3.1)

where g is the gravitational constant, Q_g is the volumetric flow rate at the diffuser, and α is the entrainment coefficient, taken as 0.083. Comparing the length scale, D, and the distance from the diffuser to the field of view (51.4 cm), the inertial particle plume should be well within the asymptotic region.

The plane of observation was illuminated from the right by a 6 Watt Argon-Ion laser. A high-speed Phantom camera with a resolution of 1024 by 1024 pixels captured a 12.4 by 12.4 cm region every 2.22 ms (450Hz) with an exposure time of 200 μs. The Phantom camera captures and stores 2,000 images (2 GB of data) during the experiment with a total of 10,000 images captured for each case. The plume is placed asymmetrically in the field of view since the larger particles (2.0 mm) interfere with PIV by creating shadows to the left. As a result, this chapter only presents the data up to the plume centerline.

3.3 Analysis

Before PIV analysis of the captured images can occur, the inertial particles must be removed using image processing techniques. This pre-processing removes the inertial

particles based on size and brightness, leaving only the seeding particles which move with the liquid phase of the plume. Figure 3.1 shows a portion of a raw image (a) before processing and (b) after image processing. The large bright objects in Figure 3.1 (a) are the 2 mm inertial particles illuminated by the laser within the field of view, while the large ghostly grey particles are inertial particles out of the field of view that are illuminated from light reflecting off the inertial particle plumes within the field of view. The inertial particles in the field of view are eliminated by a size filter while the ghostly inertial particles are removed using a brightness criteria, leaving images with only seeding particles as shown in Figure 3.1 (b). The PIV analysis is performed in DaVis (LaVision 2002) using a multi-pass cross-correlation PIV analysis of decreasing interrogation window sizes, 32 by 32 pixel to 16 by 16 pixel, with 50% overlap. This analysis resulted in velocity vectors on an 8 by 8 pixel grid corresponding to a 0.97 by 0.97 mm grid. Errant vectors are removed using a median filter which compares the value of a vector with the root mean square of neighboring vectors. Due to the removal of the inertial particles and errant vectors, the velocity fields are missing some velocity vectors. These missing velocity vectors are interpolated using a kriging interpolation scheme, which was completed using the **DACE** Matlab® toolbox (Lophaven et al. 2002). Figure 3.2 shows an example of a final velocity field from Case A. The final velocity fields are used to calculate the vorticity and local swirl strength, defined as the imaginary portion of the eigenvalue of a two-dimensional velocity gradient tensor (Adrian et al. 2000). The local swirl strength has been shown to identify vortices in the flow, working well even in regions of high shear. The vorticity field (subplot a) and local swirl

strength field (subplot b) for the velocity field in Figure 3.2 are shown in Figure 3.3. The instantaneous vorticity map in Figure 3.3 shows pockets of high vorticity in the plume region between -20 and 20 mm while the local swirl strength (subplot b) also shows the identification of vortices in the plume region. By matching the local swirl strength contours with the corresponding vorticity field, the size, circulation, and enstrophy of each vortex identified in the flow can be calculated (Bryant et al. 2009).

a)   b)
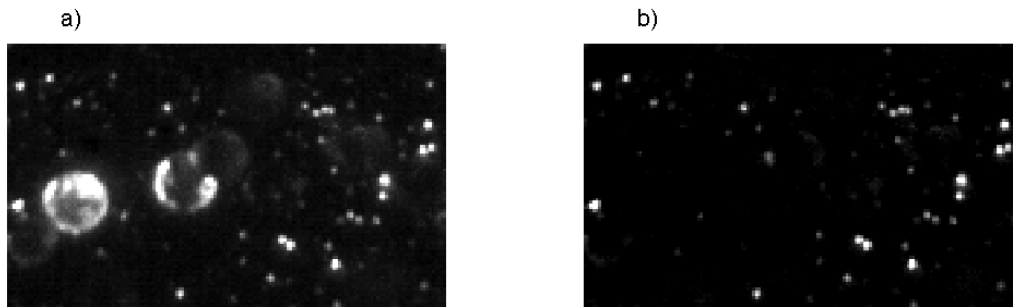
Fig. 3.1. Portion of a raw image before (a) and after (b) being processed for inertial particle removal.

Fig. 3.2.　　　Instantaneous velocity field in an inertial particle plume for Case A.
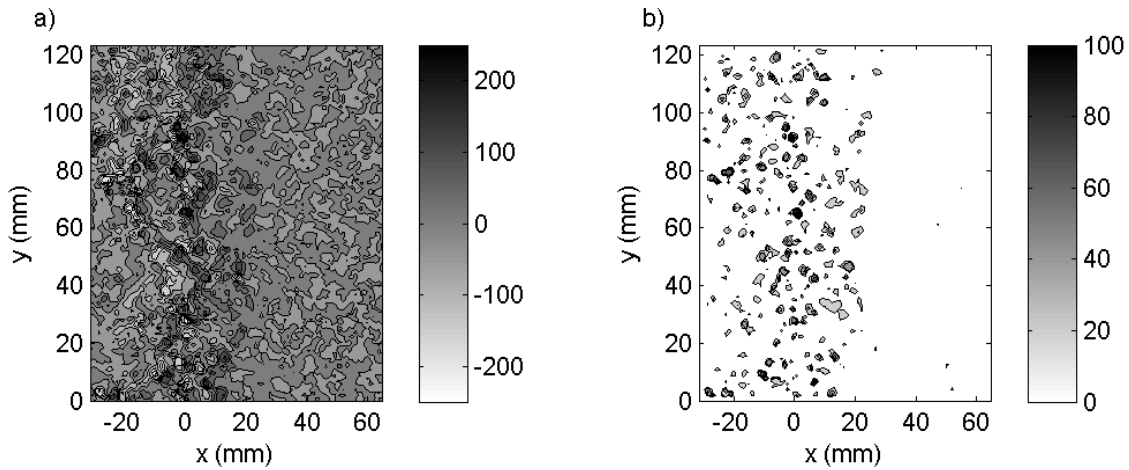
Fig. 3.3. Instantaneous vorticity field (a) and map of identified vortices showing contours of swirl strength (b) for the velocity field shown in Figure 3.2.

3.4 Results

3.4.1 Time-Averaged Properties of the Flow Field

The velocity fields are used to find both the mean and turbulent properties of the inertial particle plumes, including the identification and quantification of individual vortices. Figure 3.4 gives the void fraction of the dispersed phase for the nine experimental cases compared with the 1.0 L/min bubble plumes data taken from Bryant et al. (2009), henceforth referred to as Case X. The horizontal position is nondimensionalized by the plume radius r. The data shows the void fraction of the inertial particle plumes to have a much steeper slope than that of the bubble plumes. This is due to the drafting and grouping of the inertial particles. The nondimensional time-averaged velocity (subplot a) and vorticity (subplot b) profiles are shown in Figure 3.5. Velocity profiles are nondi-

a)
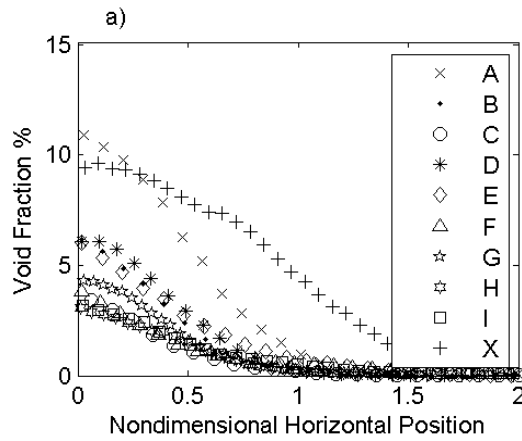
Fig. 3.4. Void fraction for all experimental cases compared with bubble plume data.

mensionalized by the time-averaged centerline vertical velocity v_c and the plume radius *r,* whereas, the vorticity plot is nondimensionalized by the absolute value of the time-averaged centerline velocity and plume radius. This difference in nondimensionalization allows for the inertial particle plume data and bubble plume data to be compared. The plume radius is found as the distance from the plume center to the point at which the time averaged velocity is 1/e of v_c.

Figure 3.5 shows the nondimensional time-averaged vertical velocity profiles are self-similar and fit a Gaussian distribution for the measured mass flow rates. The vorticity profiles (subplot b) are self-similar for the inertial particles plumes, but do not match the bubble plume data (Case X) within the measured buoyancy fluxes. The inertial particle plumes have a peak vorticity at half the plume radius whereas the bubble plume data has the peak vorticity at the plume edge, $r = 1$.
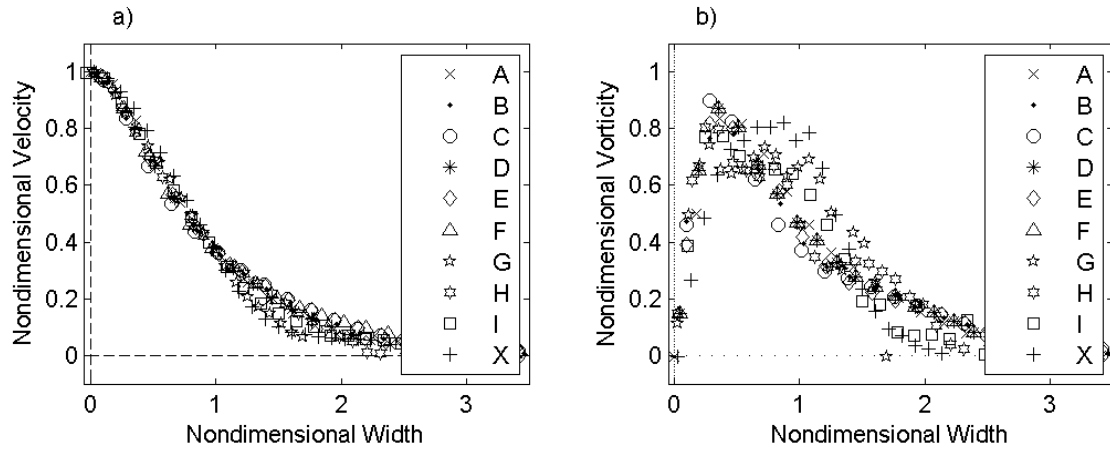
Fig. 3.5. Average nondimensional velocity profile (a) and nondimensional vorticity profile (b) of the inertial particle plumes for all experimental cases compared and bubble plume data.

One noticeable difference between the inertial particle plumes and bubble plumes, besides the mass of the dispersed phase, is the ratio of the dispersed phase radius and the plume radius, denoted as λ. The inertial particle plume test all had λ values ranging from 0.29 to 0.57 as seen in Table 3.2 while the bubble plumes had lambda values from 0.77 to 0.91. Thus, the value of maximum vorticity occurs at the edge of the dispersed phase and not at the edge of the plume though in the case of the bubble plume these values are near unity.

Table 3.2.   Characteristics of each inertial particle plume case.

Case	v_c (m/s)	r (m)	λ	E_l/r
A	-0.57	0.022	0.57	0.97
B	-0.53	0.021	0.52	1.13
C	-0.41	0.021	0.40	1.05
D	-0.44	0.025	0.54	0.84
E	-0.27	0.021	0.64	1.06
F	-0.21	0.022	0.61	0.98
G	-0.30	0.044	0.56	0.48
H	-0.24	0.036	0.52	0.52
I	-0.19	0.028	0.52	0.67

3.4.2   Characteristics of Identified Vortices

The probability of the nondimensional vortex size for each inertial particle flow rate

(subplot a) along with the average nondimensional vortex size versus position in the

plume (subplot b) is presented in Figure 3.6. The vortex size, which corresponds to the

surface area in the PIV cross-section, is nondimensionalized by the plume radius r

squared. As expected, the occurrence of large vortices is much smaller than that of small

eddies, agreeing with the concept of turbulent energy cascade. Subplot (a) shows that

the distribution of vortex size collapses into a single PDF for the cases corresponding to

the 2.0 mm and 1.45 mm particles (Cases A through E). However, the 1.0 mm cases do

not collapse but are similar to the bubble plume cases. Furthermore, subplot (b) shows

the average vortex size is also similar for the 2.0 mm and 1.45 mm particle size, and the

largest vortices exist between 0.5 and 1.0 of the plume radius in the region of highest

vorticity seen in Figure 3.5. The average size of the vortices diminish after the plume

edge due to the lack of turbulent energy input from either the inertial particle wake or

shear layer instabilities. The generating mechanism of vortices in the plume center could be either shedding from inertial particles or shear layer instabilities while those outside the plume center can be attributed to shear layer instabilities. In addition to the average vortex size, the maximum vortex size can be found. Figure 3.7 shows the nondimensional maximum vortex size versus position in the plume with peak values around 0.8 and 0.25 times the radius of the plume for the 2.0 and 1.45 mm particle sizes and 1.0 mm particle size, respectively. As with the average vortex size, the largest vortices occur in the region of greatest vorticity and then reduces after the plume edge. The length scale of the largest vortices, E_1, should be similar to the integral length scale, L_1. E_1 is defined as the equivalent diameter of the maximum vortex area found for each flow case. The values for E_1 are presented in Table 3.2 along with time-averaged centerline velocity, v_c, plume radius, r, and ratio of dispersed phase to plume radius, λ. It is expected that the inertial particles would reduce the largest vortex size as the bubbles did in Bryant et al. (2009). However, Table 3.2 shows that the maximum vortex size length scale for the 2.0 mm and 1.45 mm particle size are equal to that of the plume radius. The explanation for this difference is made clear by comparing the mass and movement of the dispersed phases. Bubbles compared to water have virtually no mass and thus no inertia, resulting in their movement being governed by vortices already in the fluid or shedding from the bubbles. This results in a flow field with bubbles being evenly spaced and having little interaction such as collisions or drafting. However, the particles used in this experiment have two and a half times the mass of the continuous phase, resulting in their movement being governed by a highly dynamic model. The

inertial particles unlike the bubbles are observed colliding, drafting, and swarming. This highly dynamic trajectory of particles increases the intermittency resulting in regions with very few particles larger than the plume radius, allowing for large vortices on the order of the plume radius to form thought only for a short period.
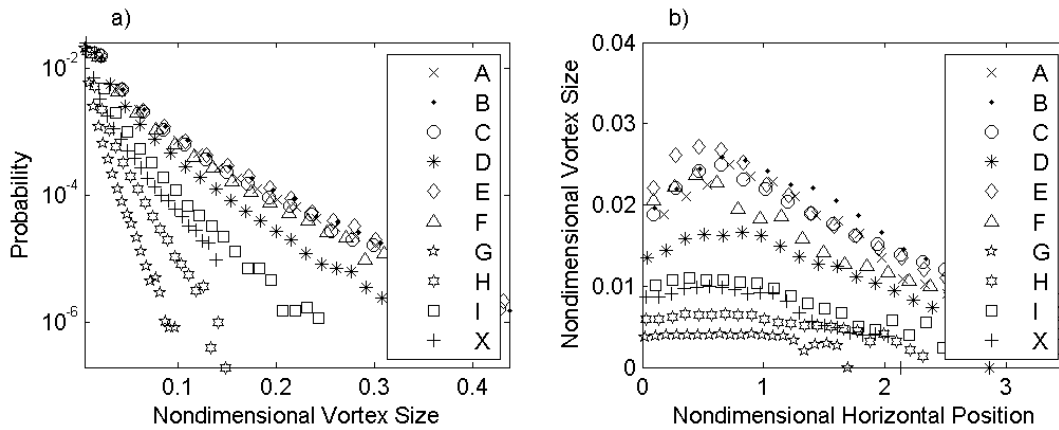
Fig. 3.6. Average probability distribution function for nondimensionalized vortex size (a) and average vortex size versus position in the plume (b) for all cases and bubble plume data.
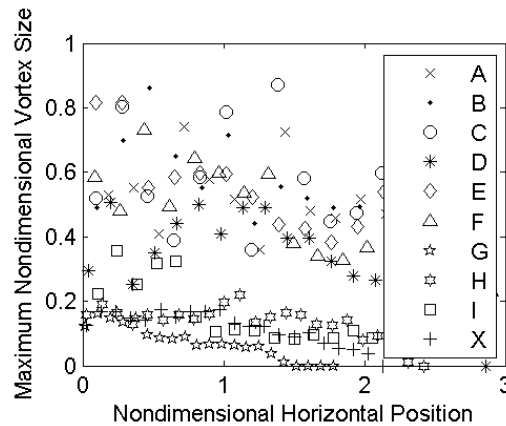
Fig. 3.7. Maximum nondimensional vortex size versus nondimensional horizontal position in the plume.

The circulation and enstrophy were also calculated to provide an understanding of the mixing and energy potential of the identified vortices. Figure 3.8 depicts the nondimesional average circulation (subplot a) and enstrophy (subplot b) for each vortex versus the nondimesional plume position. Nondimesionalization of the circulation was achieved by dividing the circulation by the plume radius r and centerline velocity v_c with the enstrophy being nondimesionalized by v^2_c alone. As with the maximum vorticity, the maximum vortex circulation occurs at half the plume radius, but the bubble plume data shows the maximum vortex circulation occurring at the plume radius. At the plume center the average circulation is zero since the vorticity changes sign, but by looking at the average enstrophy in (subplot b), it is shown that the vortices in the plume center are the most energetic for all cases of inertial plume. It is unclear whether the energy in the vortices in the plume center is related to vortex shedding or produced in continuous phase turbulence. As with the circulation, the enstrophy results are different from the bubble plume data and can be contributed to the higher velocity in the particle plumes and the difference in the boundary layer of bubbles and particles. The average circulation and enstrophy of identified vortices outside the plume radius are much smaller since there is little input energy.

The combination of Figures 3.6 and 3.8 result in Figure 3.9 illustrating the correlation of the magnitude of the vortex circulation (subplot a) and enstrophy (subplot b) with vortex size. The figure shows a strong relationship between the vortex size and its circulation and enstrophy. The 2.0 mm and 1.45 mm particle plumes have good agre-
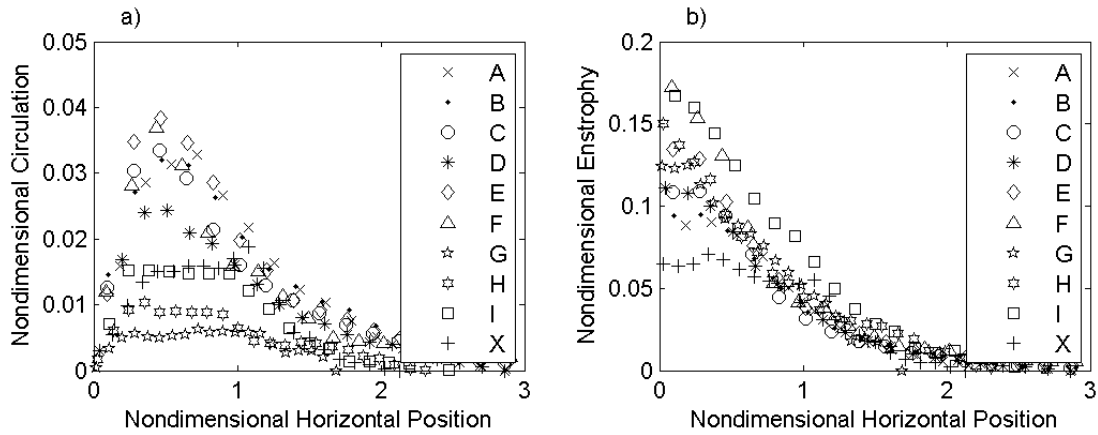
Fig. 3.8. Average nondimensional circulation (a) and enstrophy (b) versus plume position for all cases and bubble plume data.

ement with one another while the 1.0 mm particle plumes appear to exist in another dynamical regime. A comparison with the bubble plume data splits the two regimes suggesting that the 1.0 mm particles' inertia is below a critical value. To check the convergence of these turbulent results, a comparison was made between the data from one experiment (4.4 s) and the average for three experiments (13.3 s) for Case A. Figure 3.10 shows the comparison for the nondimesional average vortex size (subplot a) and nondimesional average circulation (subplot b) versus nondimensional horizontal position. This figure shows the convergence of the turbulence data, ensuring the accuracy of the time-averaged turbulence results.
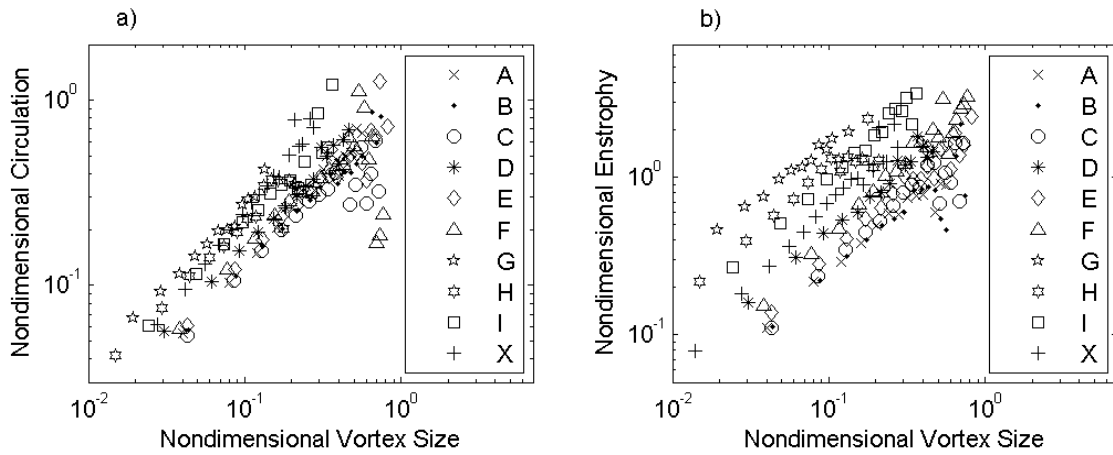
Fig. 3.9. Comparison of nondimensional vortex size versus nondimensional circulation (a) and enstrophy (b).
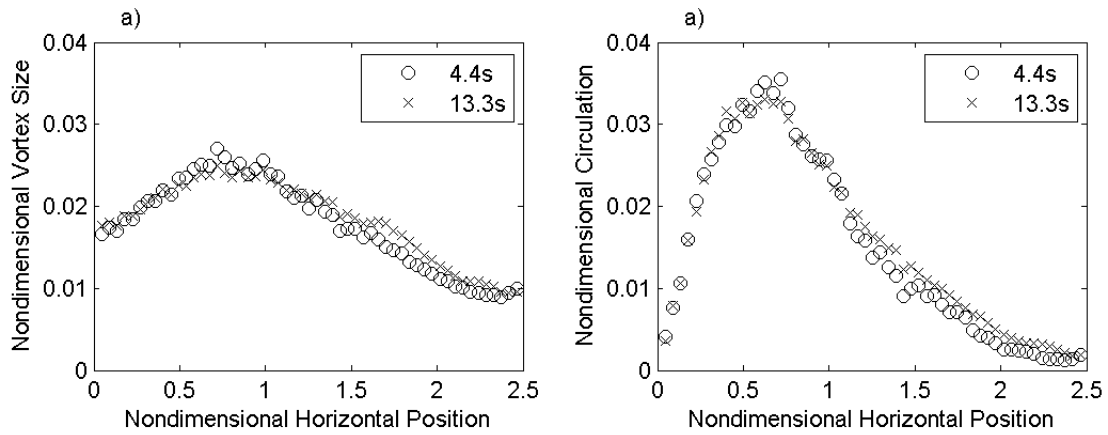
Fig. 3.10. Comparison of the nondimensional vortex size (a) and nondimensional circulation (b) for 4.4 and 13.3 s worth of data versus the nondimensional horizontal position for Case A.

3.4.3   Turbulence Statistics

Expanding beyond average vortex properties, this section presents more typical turbulent measurements, turbulent stresses and energy spectra. Figure 3.11 presents the profiles of the nondimensional time-averaged turbulent stresses versus nondimensional plume position.   The turbulent stresses are nondimensionalized by the local time-average velocity $v(x)$ shown in Figure 3.5. The nondimensional turbulent stress increases from the center to the plume edge. The turbulent stresses for the inertial particle plumes are all similar in the plume region, but the bubble plume data is much smaller in the vertical turbulent stresses, $v'v'$. This can be attributed to how turbulence is generated from the bubbles and particles and their respected boundary layers. Outside the plume ($r > 1$), the agreement between the turbulent stresses is affected by the velocity of recirculation regions in the tank.

Figure 3.12 presents the autocorrelation functions and turbulent energy spectra for the 2.0 mm particle size cases. These results for the 1.45 and 1.0 mm particles are presented in Figure 3.13 and 3.14, respectively. These figures present the results for three different plume locations: the plume center line (subplot a and d), the midpoint between the plume center line and plume edge (subplot b and e), and the plume edge (subplot c and f). The autocorrelation of the fluctuations for the vertical component v'
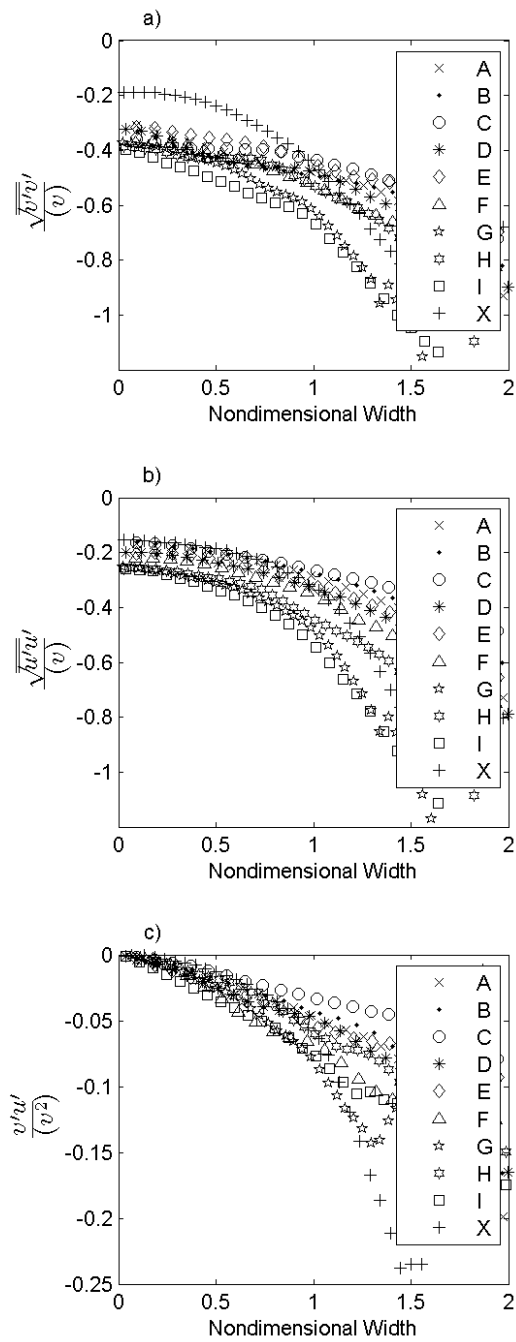
Fig. 3.11. Average nondimensional turbulent stress versus position in the plume for all cases and bubble plume data.

are given in column 1. As with the bubble plume data presented by Bryant et al. (2009), the presence of a dispersed phase changes the curvature of the autocorrelation function at zero lag compared with the continuous phase where no particles or bubbles are present. The integral time scale can be found by first integrating the autocorrelation functions up to the point at which the correlation becomes negative. The characteristic length scale L_1 is found by multiplying the integral time scale by the local time-averaged velocity. Table 3.3 gives the nondimesional value of L_1 for each mass flow rate at each of the three positions and was used to nondimensionalize the energy spectra in Figures 3.12, 3.13, and 3.14. The table shows the nondimensional length scale to be approximately equal to the plume radius for the 2.0 mm particles, three quarters the plume radius for the 1.45 mm particles, and just under half the plume radius for the 1.0 mm particles. A comparison of the vortex length scale E_1 with the characteristic length scale L_1 shows similar estimates of the characteristic length scale generally being below that of the vortex length scale.

The energy spectra in Figures 3.12, 3.13, and 3.14 are the average of the energy spectra for each 4.4 s image captured from the experiments. The Reynolds stress $\overline{v'^2}$ and the characteristic length scale are used for the nondimesionaliztion of the turbulent energy spectra. Along the plume center, the turbulent energy spectrum was found to have a slope more closely to -7/6 (bold solid line) than the classical -5/3 (bold dashed line). This slope has been identified in the inertial subrange in bubbly flows by Lance and Bataille (1991), Rensen et al. (2005), and Bryant et al. (2009). However, along the plume edge where there is little to none of the dispersed phase (inertial particles), the turbulent energy spectra closely matches the classical slope of -5/3. This study does not resolve the dissipation range where a dispersed phase has been shown to change the slope to between -8/3 and -11/3 (Lance and Bataille, 1991). This modulation in the turbulent energy spectra is associated with the input of turbulent energy at a separate length scale, the length scale of the dispersed phase rather than that of the integral length scale as explained by Balachandar (2009).
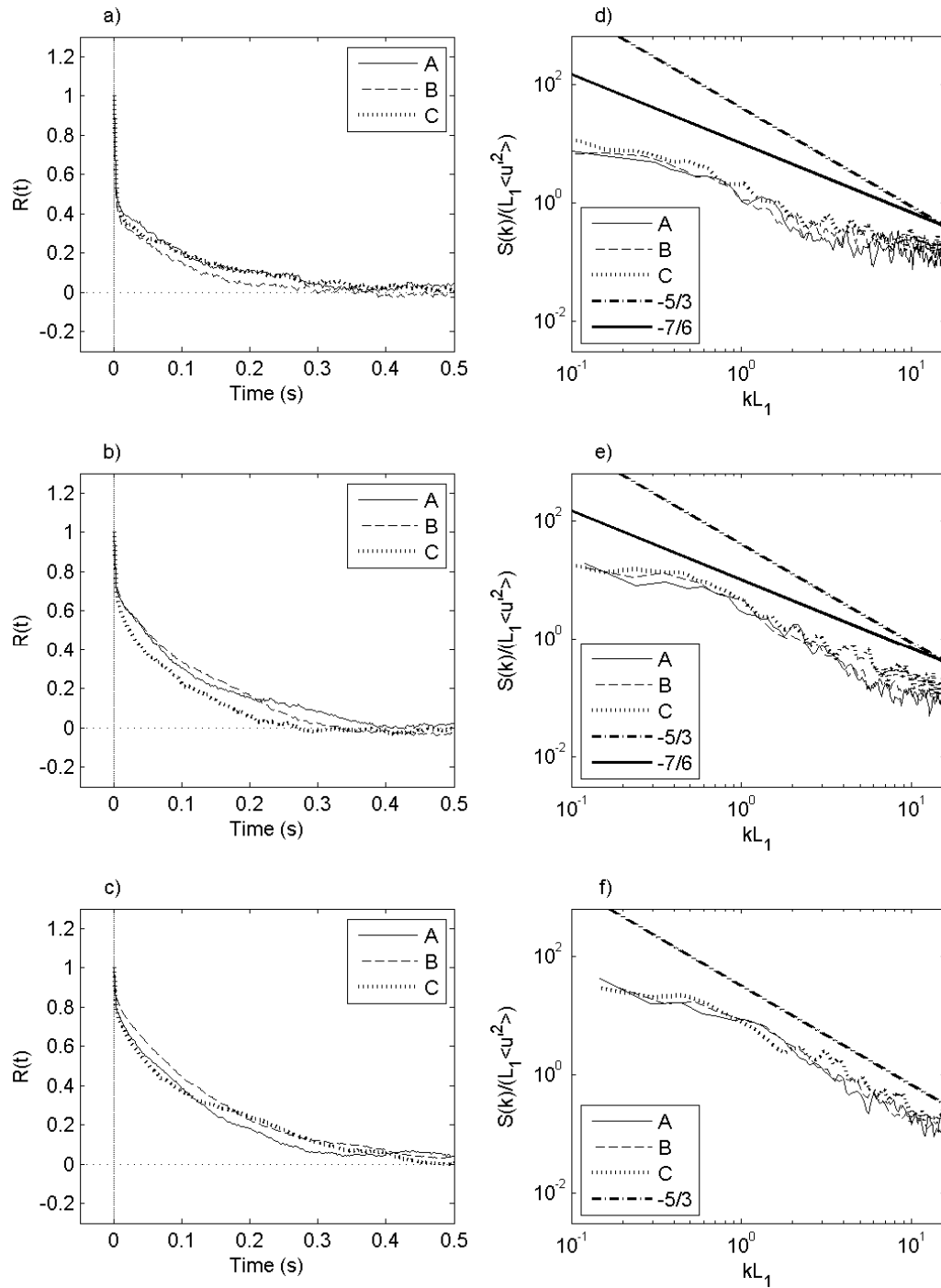
Fig. 3.12. Autocorrelation function of the turbulence and nondimensionalized turbulent energy spectrum for three positions in the plume: (a and d) plume center, (b and e) midpoint between plume center and plume edge, and (c and f) plume edge for all Cases A, B and C.
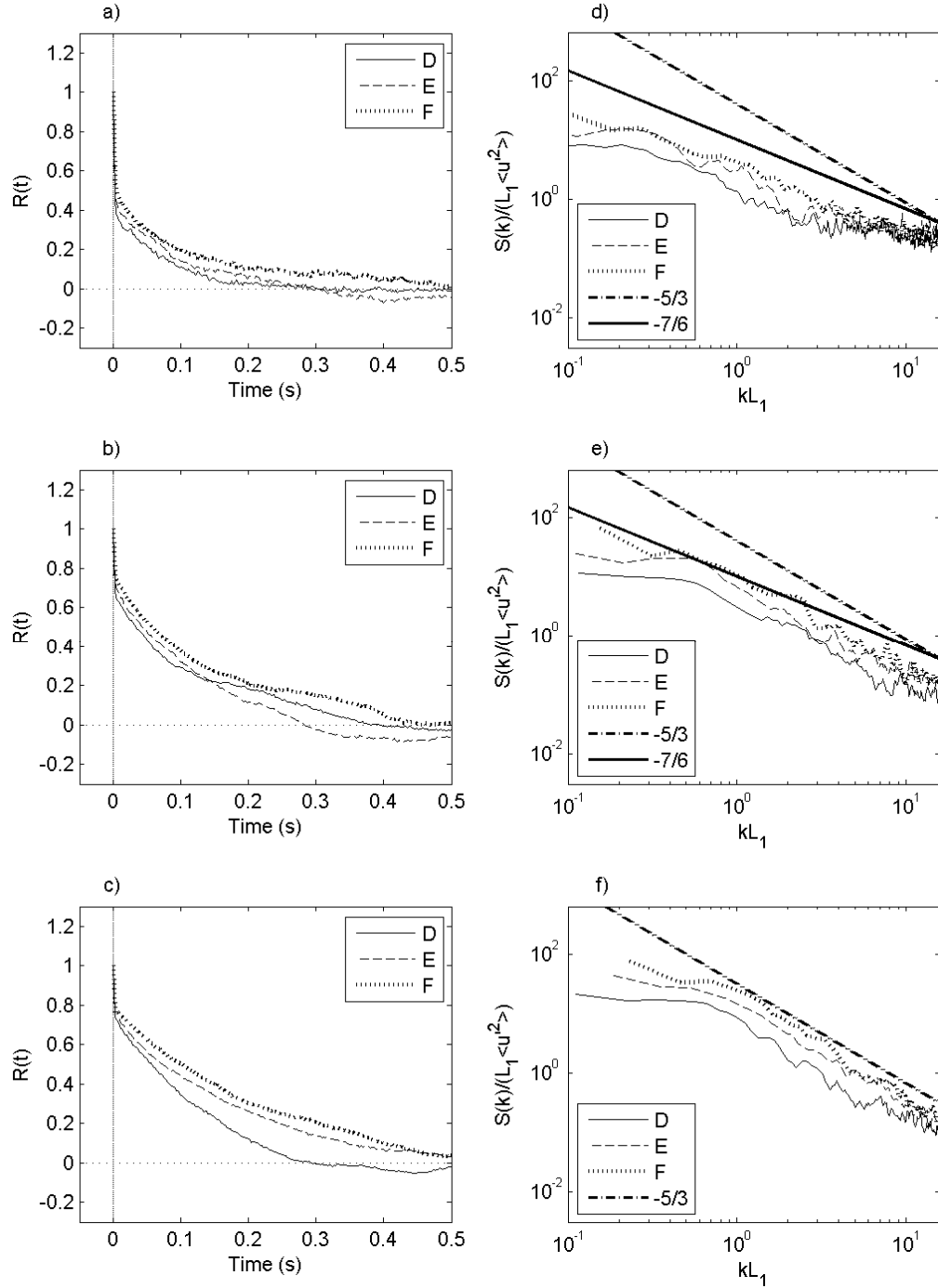
Fig. 3.13. Autocorrelation function of the turbulence and nondimensionalized turbulent energy spectrum for three positions in the plume: (a and d) plume center, (b and e) midpoint between plume center and plume edge, and (c and f) plume edge for all Cases D, E and F.
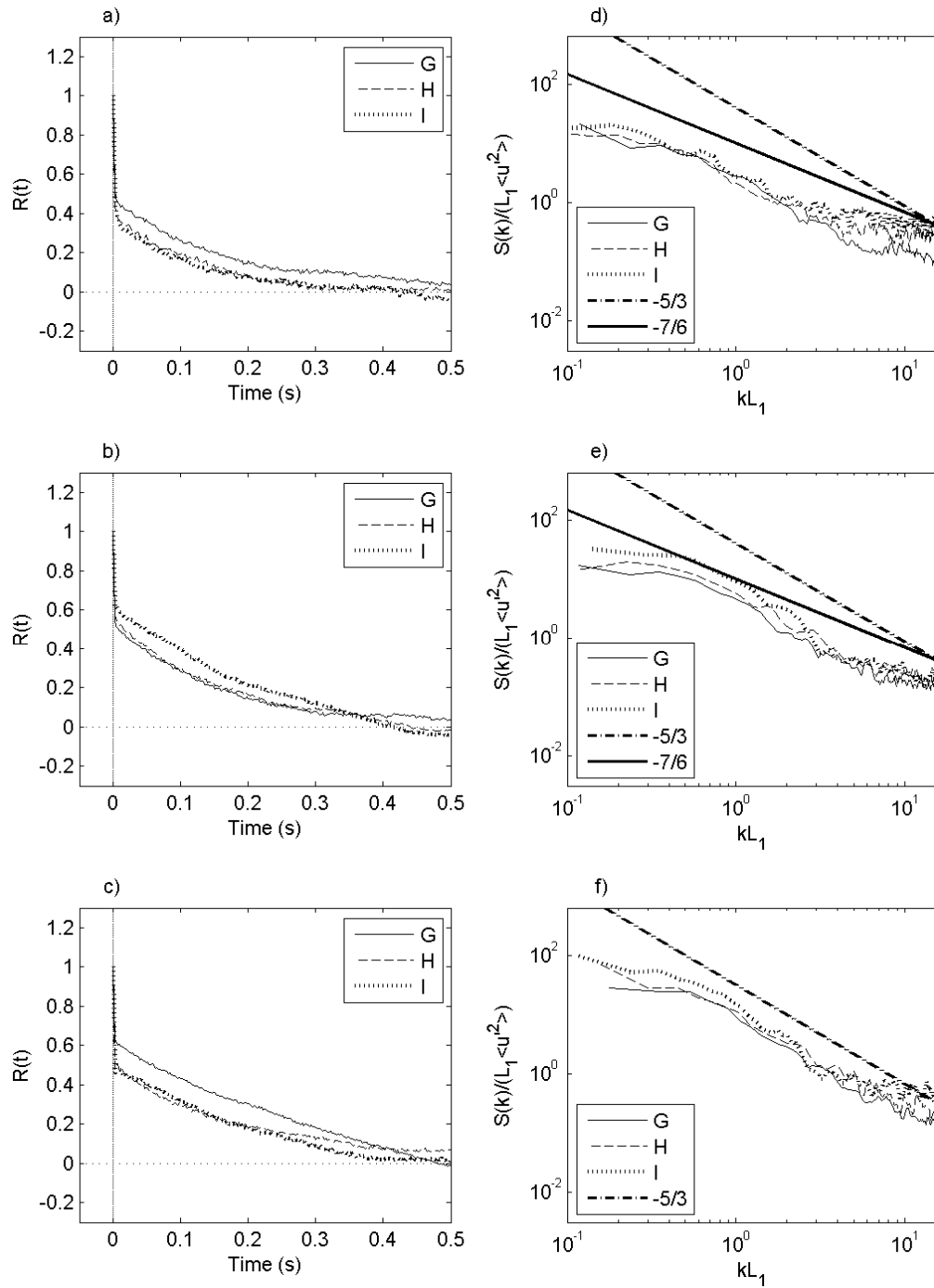
Fig. 3.14. Autocorrelation function of the turbulence and nondimensionalized turbulent energy spectrum for three positions in the plume: (a and d) plume center, (b and e) midpoint between plume center and plume edge, and (c and f) plume edge for all Cases G, H and I.

Table 3.3.   Characteristic length scale L_1 for each case reported at the plume center (a), midpoint between the plume center and edge (b), and at the plume edge (c).

| Case | L_1/r | | |
	(a) Plume Center	(b) Midpoint Between Center and Edge	(c) Plume Edge
A	1.40	1.50	0.99
B	0.93	1.35	1.19
C	1.09	0.68	0.85
D	0.53	1.04	0.62
E	0.52	0.66	0.62
F	0.62	0.68	0.58
G	0.56	0.42	0.34
H	0.32	0.37	0.28
I	0.30	0.46	0.18

3.5 Summary and Conclusions

This chapter presented a high-speed PIV study of inertial particle plumes for particle diameters of 2.0, 1.45, and 1.0 mm. Three different mass flow rates were used for each particle size to drive the flow as a Phantom camera captured a 12.4 by 12.4 cm region. Pre-processing image analysis based on the brightness and size of particles was successfully used to remove the inertial particles before the PIV analysis. After PIV analysis, error vectors were removed with missing vectors interpolated using a kriging algorithm. The resulting velocity fields were used to find the vorticity and local swirl strength fields, which when combined allowed for the identification and quantification of vortices in the flow. The average vortex properties were presented along with the turbulent stresses and energy spectra. This data was further compared to bubble plume data.

Nondimensionalization of the flow properties were achieved using the time-averaged centerline v_c velocity and plume radius r. However, this was not completely successful in collapsing the data as the particle's inertia was also an important parameter. The data showed the time-average velocity profiles to have a Gaussian distribution while the maximum vorticity occurred along the edges of the dispersed phase, which for the tested cases were one half the plume radiuses.

The average vortex properties showed the vortices with the greatest size and circulation also present at one half the plume radius, while the most energetic vortices occurred in the core of the plume. This differed from the comparable bubble plume data which had the most energetic vortices along the plume edge in the shear layer. The maximum vortices found in the flow were also larger than those found in bubble plumes. This difference is associated with the intermittency of the inertial particles whose trajectory is influenced by drafting and swarming. The smaller particles, 1.0 mm, had smaller vortices which were similar to that of bubble plumes.

Finally, the turbulent energy spectra of the plumes in three different locations were compared. As with other multiphase flows, the slopes of the spectra were modulated in the region with the dispersed phase to -7/6. This change was in agreement with bubbly flow studies. However, the mechanism for this change, either the acceleration around the particles or the vortex shedding, was not able to be identified. This study shows the dynamics of inertial particle plumes to be similar to bubble plumes.

CHAPTER IV

FORMATION OF TIDAL STARTING-JET VORTICES THROUGH BAROTROPIC

INLETS WITH FINITE LENGTH

This chapter presents a surface particle image velocimetry study conducted to investigate the influence an of expelled lateral boundary layer vortex on the growth and propagation of a tidal starting-jet vortex. The physical model was tested in a 15 by 5.5 meter, shallow water basin with two CMOS cameras imaging a 2.75 meter by 1 meter region at 16 Hz for over 4 tidal cycles of 50 seconds each. A local swirl strength criterion was applied to the continuous surface velocity fields to identify large two-dimensional vortices in the flow. The identified flow structures were characterized by their trajectory, size, and circulation. Using these quantities, a model was developed to predict the size and strength of the expelled lateral boundary layer vortices based on the inlet velocity, channel length, and width of the lateral boundary layer. The expelled boundary layer vortices were found to disrupt the formation of the tidal starting-jet vortices through two mechanisms. Because the boundary layer vortex forms a dipole with the starting-jet vortex, the starting-jet vortex propagates away from the inlet mouth resulting in a reduction in the spin-up time and the amount of vorticity input during its formation. In addition, the lateral displacement of the dipole removes the starting-jet vortex from the shear layer between the ebb tidal jet and the ambient fluid, which would continue to strengthen the vortex beyond the initial spin-up time. These changes in the starting-jet vortices' formation and propagation are found to be a function of the channel

length *L*, maximum velocity *U*, and tidal period *T*, resulting in a predictive non-dimensional value to characterize the trajectory.

4.1 Introduction

Estuaries and surrounding coastal systems are important for marine habitat, shipping, and recreation, and they are often composed of complex fluid flows. These systems serve as the spawning and maturing grounds for larvae and young fish (Roughan et al. 2005) and are important to the dispersion of suspended nutrients and containments (Chadwick and Largier 1999a). One particular flow feature in inlet systems are starting-jet vortices that form due to tidal flows which impact estuary flushing (Van Senden and Imberger 1990). Although studies have been conducted to understand the formation and propagation of starting-jet vortices using highly idealized inlets (Wells and van Heijst 2003; Nicolau et al. 2009), by varying the channel length, this chapter aims to quantify the mean and turbulent vortex properties, and identify the mechanics influencing tidal starting-jet vortices affected by lateral boundary layers expelled from an inlet channel.

Vortex dynamics in shallow water flows have been extensively studied using both experimental and numerical methods. Since starting-jet vortices in shallow water have a horizontal length scale much greater than the water depth, they are classified as two-dimensional large coherent structures (Jirka 2001). The generation of a tidal vortex is formed by the flow separation from the lateral boundary which transports high vorticity (Signel and Geyer 1991) or by the transport of vorticity from the inlet channel, rolling up to create a vortex (Wells and van Heijst 2003).

Field studies of tidal vortices at inlets and headlands were conducted using acoustic Doppler current profilers (ADCP) by Pawlak et al. (2003), Geyer and Signell (1990), Geyer (1993), and Old and Vennell (2001). Additionally, van Senden and Imberger (1990) used a CTD (conductivity, temperature, and depth) profiler in combination with drifters to study the growth and quasi-steady phase of tidal vortices. These studies identified tidal vortices and associated properties, such as upwelling, but were unable to acquire high spatial resolution data.

Numerical studies of ocean and coastal flows are often employed due to the difficulty of field experiments and scaling requirements for laboratory experiments. A numerical model study of flow around headlands using a depth integrated vorticity equation was performed by Signell and Geyer (1991). Flow through an inlet is inherently different than flow around headlands in that the produced vortex from an inlet has an identical, opposite-rotating vortex across the channel that results in self propagation by dipole formation (Wells and van Heijst 2003). However, Signell and Geyer (1991) demonstrated the successful use of a depth integrated model to capture the generation and propagation of large 2-D coherent structures with variations in three important length scales controlling the flow: frictional length, tidal excursion, and headland length. Furthermore, tidal generated starting-jet vortices through an inlet were studied using Boussinesq-type equations (Kim et al. 2009) which yielded predictions of the position of the vortices in time.

To reinforce the results from numerical models, laboratory experiments have been conducted. Laboratory experiments were conducted by Lin et al. (2003) studying

starting-jet vortices formed from a jet in shallow water with a free surface boundary, showing the evolution of the vortex in time with varying water depth. This study also captured the three-dimensionality of large two-dimensional starting-jet vortices but did not consider the reversing tide or an expelled boundary layer vortex. Starting-jet vortices considering the effect of the reversing tide through an inlet have also been studied experimentally. Kashiwai (1985a, and 1985b) conducted large scale experiments in a 5m by 5m basin and used floats to determine the qualitative flow pattern. Wells and van Heijst (2003) conducted dye experiments in stratified fluid, minimizing bottom friction effects, and found that three different tidal starting-jet vortex conditions exist based on the inlet Strouhal number K_w calculated as the ratio W/UT where W is the tidal inlet width, U is the maximum velocity through the inlet, and T is the tidal period. The inlet Strouhal number can be seen as the ratio of the sink length scale, l_s, to the jet excursion length scale, l_j, and are presented in del Roure et al. (2009).

Though previous studies have successfully predicted the flow pattern (Wells and van Heijst (2003) and Kim et al. (2009)), these studies did not investigate the effect the channel length (expelled lateral boundary layer) has on the generation and propagation of tidal starting-jet vortices. Figure 4.1 shows the resulting flow pattern from the idealized cases of zero inlet length. For inlets of finite length, a lateral boundary layer forms in the tidal inlet during both the ebb and flood tide and has a region of recirculation as shown in previous studies by Kashiwai (1985a) that is expelled from the inlet channel during the reverse flow and is illustrated in Figure 4.2. The recirculation

region's rotation is opposite that of the generated starting-jet vortex resulting in a pair of dipoles.
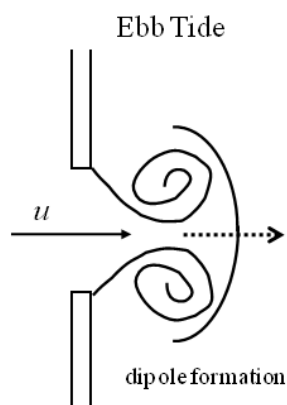
Fig. 4.1.   Flow pattern of starting-jet vortices without the influence of an expelled boundary layer.
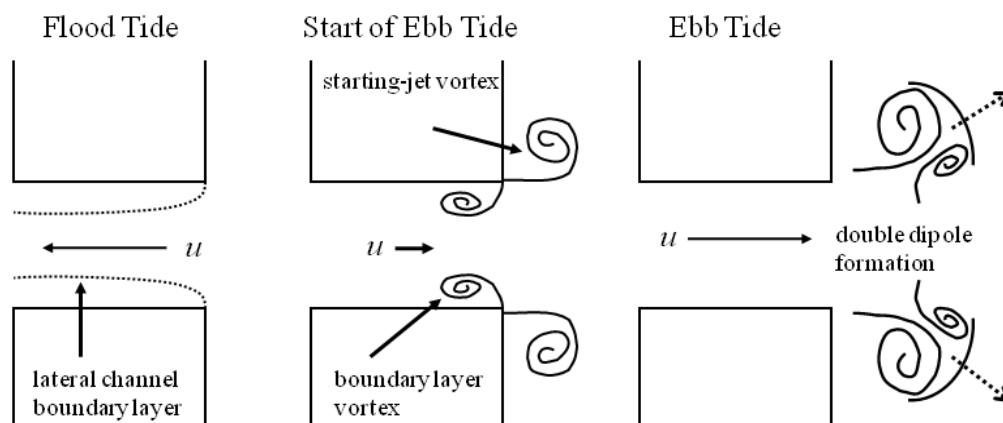
Fig. 4.2.   Pattern of starting-jet vortices and expelled boundary layer vortices for flow through an inlet with finite channel length.

Tidal inlet channels or barriers islands often have a channel length on the order of or larger than the channel width requiring the understanding of the lateral boundary layer. This chapter presents a large scale, physical model, surface particle image velocimetry (PIV) study performed to investigate the generation and propagation of starting-jet vortices with the influence of an expelled lateral boundary layer. The following section will detail the physical model and the procedures used in data collection and analysis. Results from the six different physical models are presented in the Results section, while the Discussion section will draw on these results to predict the strength of the expelled boundary layer vortices and the starting-jet vortices, and the trajectory angle of the starting jet-vortices.

4.2 Description of Experiments and Analysis

4.2.1 Setup of Physical Model

Surface particle image velocimetry (PIV) experiments were conducted in a shallow water basin, 15 m by 5.5 m, at the University of Karlsruhe, Institute for Hydromechanics, in Karlsruhe, Germany. For all experiments performed, the water depth was 5 cm with the midpoint of the inlet corresponding to the basin's midpoint of 7.5 m and along the centerline of 2.75 m (Refer to Figures 4.1 and 4.2). Sinusoidal flow was generated using a programmable variable speed pump and four butterfly valves that allowed for flow reversal. The maximum velocity through the inlet, U, was 21 cm/s with a tidal period, T, of 50 s. The experiments were designed with a value of $K_w = .09$ such that the vortex would remain nearly stationary in front of the inlet on the flood tide,

described by Wells and van Heijst (2003) as Type 1, allowing for more surface particle image velocimetry data. The inlet width, *W*, was set to 94.4 cm for all experiments, and observation during the experiments showed a nearly stationary dipole on the seaward side during the first flood tide. Using the maximum velocity through the inlet, *U*, the Froude number was calculated to be 0.3, well within the subcritical flow range. The Reynolds number, Re, was 10500; hence, the tidal jet flow was fully turbulent.

Two different idealized configurations were used. The first configuration, referred to as the barrier island case, was modeled with two different inlet lengths. The first barrier island case, shown in Figure 4.3 (Layout A), had an idealized rectangular inlet with channel length of 15 cm (0.11 times the inlet width of 94.4 cm). The second barrier island case, also shown in Figure 4.3 (Layout B), had an idealized rectangular inlet with a channel length of 135 cm (1.43 times the inlet width of 94.4 cm).

Layout A: Barrier Island 0.15m   Layout B: Barrier Island 1.35m
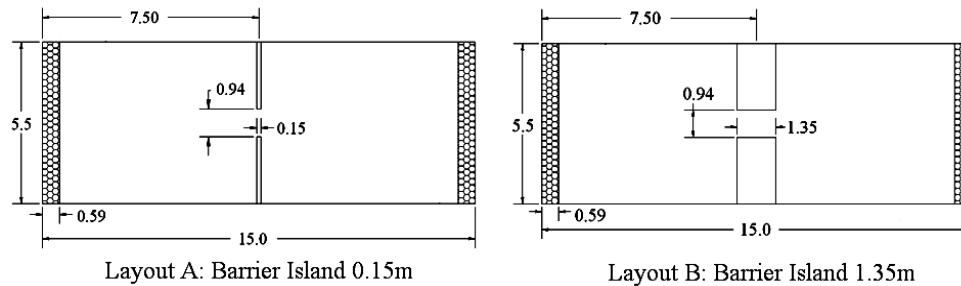
Fig. 4.3.   Barrier island cases: Layouts A and B in meters.

These two configurations allowed for the comparison between an inlet with and without a developed lateral boundary layer that was expelled during the ebb tide. The second configuration, referred to as the jetty case, modeled an idealized inlet that had

jetties on the seaward side. Four jetty lengths of 39, 63, 87, and 111 cm corresponding

to 0.41, 0.67, 0.92, and 1.17 times the inlet width and referred to as Layout C, D, E, and

F in Figure 4.4 respectively, were used to evaluate how changes in the channel length

affected the development and propagation of the starting jet vortices.
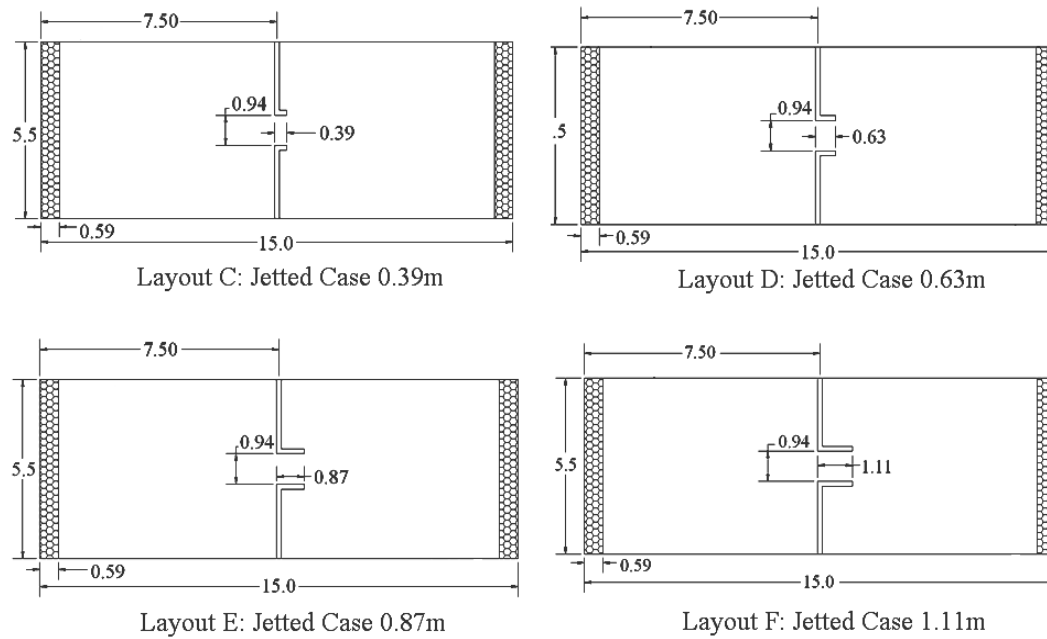
Fig. 4.4. Jetted cases: Layouts C, D, E, and F in meters.

The experiments were seeded with black floating particles that followed the flow

and contrasted well against the basin's white floor. Three halogen lights were used to

increase the ambient lighting, improving the contrast and image quality. Two 8-bit

CMOS cameras with resolutions of 1024 by 768 mounted overhead imaged the particles

at 16 Hz. The cameras were position to capture one half of the symmetric flow from the

channel centerline to 1.1 m toward the basin edge and from the barrier island to 2.84 m

seaward side with an 11 cm overlap to guarantee an uninterrupted field of view. This camera setup resulted in each pixel equaling 1.44 mm by 1.44 mm. Due to the expected symmetry of the flow, half of the flow was imaged, and videoed dye tests were conducted to confirm this assumption. Dye studies also contributed to the understanding of the flow by clearly identifying the lateral boundary layer in the inlet. The CMOS cameras captured images for over four tidal cycles and saved them real-time to a six disk RAID for 220 s, wielding 3520 frames of data per camera per experiment.

4.2.2 Image Preprocessing, PIV, and Vector Post Processing

The raw images obtained from the CMOS cameras had a white background with black particles. The images were inverted using Matlab®, and the image quality was further improved before the PIV analysis by subtracting the mean, eliminating any discontinuity in the image lighting. Images were cut so that the final velocity fields from the two camera's images could be combined into a complete continuous velocity field.

Grid plate images from each camera were used in DaVis by LaVision to correct for any lens distortion and correctly scale the inverted cut images. The scaled images were then processed in DaVis Ver. 6.2 to find the velocity vectors. A multi-pass PIV method was chosen with the first pass using a 64 pixel by 64 pixel window with 50% overlap and the second pass using a 32 pixel by 32 pixel window with 50% overlap, which resulted in a velocity vector every 2.8 cm in the field of view.

The images were masked accordingly to remove regions of the images that represented a barrier island or jetty from the vector calculations. Error vectors were removed in DaVis using a median filter and replaced with interpolated values. Figure

4.5 represents a typical velocity field resulting from the PIV analysis. This figure shows every second velocity vector (reducing the clutter) for flow during an ebb tide between two barrier islands with a channel length of 135 cm.
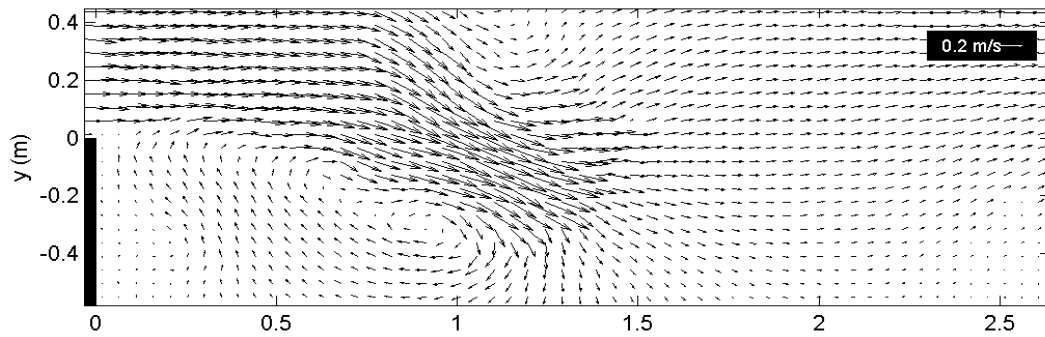
Fig. 4.5. Typical velocity field for flow between two barrier islands showing every second vector.

4.2.3 Vortex Identification and Quantification

Velocity fields were processed in Matlab® to identify vortices in the flow. Vortices were identifiied by finding the local swirl strength as defined by Adrian et al. (2000). The local swirl strength can be found by first using the two-dimensional velocity data to build an equivalent two-dimensional velocity gradient tensor, d^{2-D}, shown in Equation 4.1. Velocity gradients were found using a five-point centered method (Raffel et al. 1998).

$$d^{2-D} = \begin{bmatrix} \dfrac{\partial u}{\partial x} & \dfrac{\partial u}{\partial y} \\ \dfrac{\partial v}{\partial x} & \dfrac{\partial v}{\partial y} \end{bmatrix} \qquad (4.1)$$

The local swirl strength, related to the local rotation frequency, is the imaginary part of the eigenvalues for the velocity gradient tensor, d^{2-D}. If a region did not have an imaginary part, it did not exhibit local rotation. While both the local swirl strength and vorticity are non-zero in local rotation, vorticity is also non-zero in areas of pure shear, where there is no local rotation, making it inappropriate to identify vortices. The local swirl strength is responsive only in regions of local rotation. Figure 4.6 shows the swirl strength contours multiplied by the sign of the vorticity for the velocity field shown in Figure 3.5 and clearly shows the existence and direction of rotation of vortices in the flow. Matlab® was used to label each vortex by converting the swirl strength contours into black and white images where white represents non-zero local swirl strength.
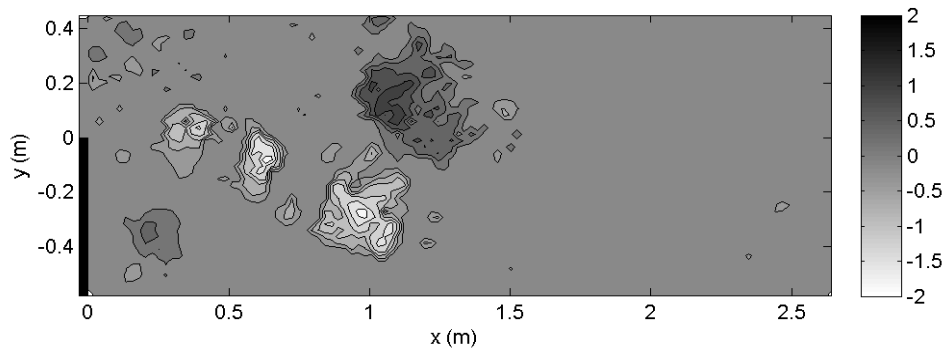
Fig. 4.6. Identification of vortices using a contour of local swirl strength multiplied by the sign of the vorticity to show direction of rotation.

The identified objects were filtered based on their size. Since the dominant flow features in coastal regions are generally two dimensional, the horizontal length scales are much larger than the vertical length scale, the smaller vortices in the flow will either be dissipated by three-dimensional turbulence or absorbed into larger two dimensional vortices. The cut-off criterion for the size was based on the calculation of an equivalent radius, removing any vortex whose equivalent radius was not twice the water depth of 5 cm (10 cm).

Remaining vortices were processed to find the trajectory, size, and circulation with the center of the vortex at the point of greatest local swirl strength. The maximum local swirl strength value, its location in space, the size of the vortex and circulation were also logged. The circulation, Γ, was calculated by summing the vorticity over the vortex's area, shown as

$$\Gamma = \int\int \omega dxdy \qquad (4.2)$$

where ω represents the vorticity. Hence, the processed data contains the time history of each vortex's trajectory and computed properties.

4.3 Results

Using the surface particle image velocimetry data and the analysis techniques described in the previous section, the response of tidal starting-jet vortices to different inlet geometries is presented. Figure 4.7 shows the trajectory (a), size (b) and circulation (c)

of the tidal starting-jet vortices for Case A every 2 seconds. The origin of the x-y coordinate system is placed at the leading edge of the inlet for all the results presented, such that x is directed offshore. Figure 4.7 clearly shows that for the tidal cycles in which data was collected, the trajectory, size, and circulation are well converged. Bolded markers in sub-plot (a) represent the position of the starting-jet vortices at slack tide (25 seconds) and this position is denoted by a vertical line in subplots (b) and (c). These experiments show little change in the size of the starting-jet vortices while it is in the field of view; however, the circulation does decay. This decay is a result of both the bottom friction and vortex stretching occurring during the flood tide. In our analysis, we consider the effect of the expelled boundary layer from a dynamical systems approach. The trajectory for this case can be characterized as a dynamical system response Mode 0, where the boundary layer represents a bifurcation to the system response. If the bifurcation (expelled boundary layer vortex) is not large enough the dynamical system response will remain Mode 0.
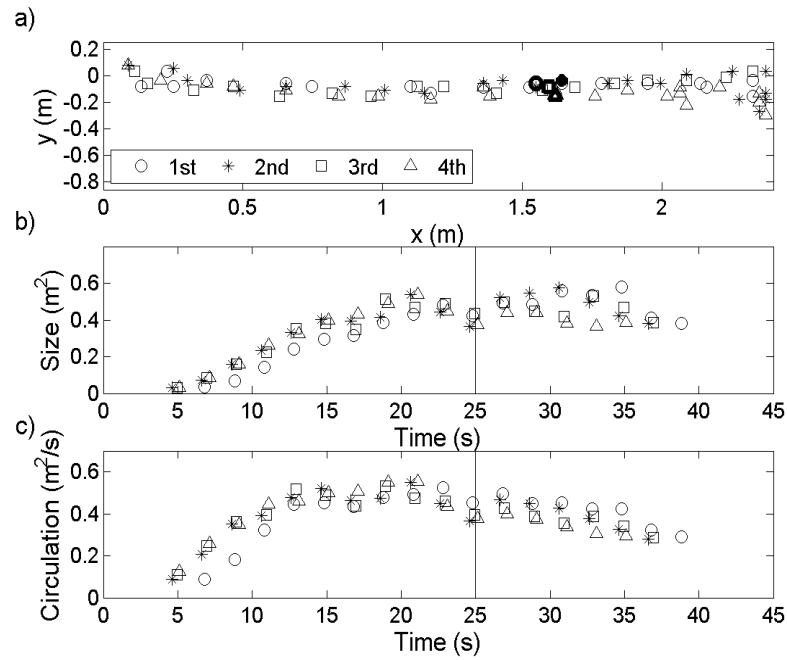
Fig. 4.7. The trajectory (a), size (b), and circulation (c) of the starting-jet vortices for tidal cycles one, two, three, and four for Case A.

As the bifurcation grows, so does the deviation from the system response Mode 0. Figure 4.8 shows the average trajectory (a), size (b), and circulation (c) of the starting jet vortex for Cases A, C, D, and E for tidal cycles 2, 3, and 4. The first tidal cycles begin in a still basin are not included since they are expected to be similar to that of Case A and do not represent a condition where an expelled lateral boundary layer exists. The figure shows that as the jetty length is increased (A being the shortest, E being the longest) the starting-jet vortices have a larger lateral deviation, slack tide position closer to the origin, and the size and circulation decrease in magnitude. The typical error bars shown for the size (b) and circulation (c) represent the standard deviation of the experimental data.
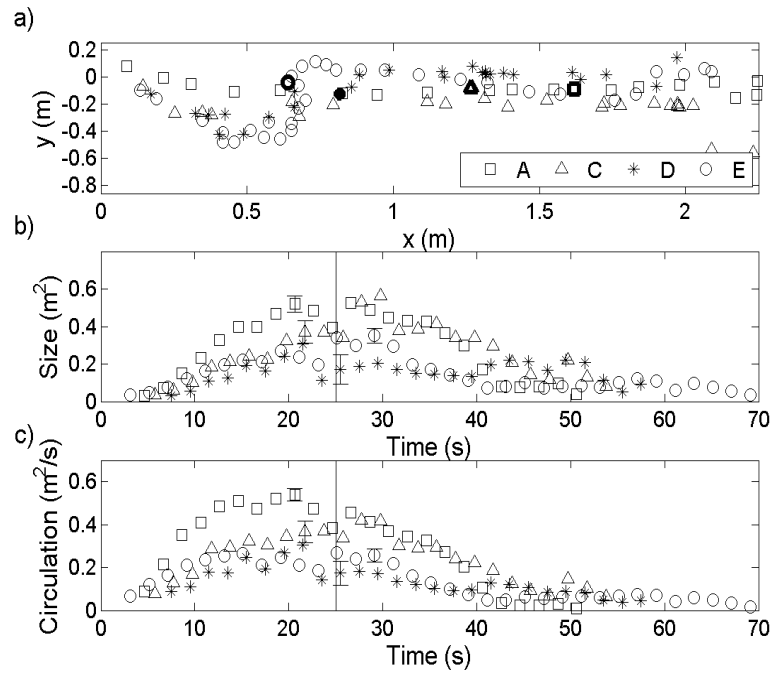
Fig. 4.8. The average trajectory (a), average size (b), and average circulation (c) of the starting-jet vortices for second, third, and fourth tidal cycles for Cases A, C, D, and E.

Similar to Figure 4.8, Figure 4.9 illustrates the results for the expelled boundary layer vortex. For Case C, an expelled boundary layer vortex is only identified for the second tidal cycle; however, the vorticity from the boundary layer is still expelled with the ebb tide resulting in a small lateral deviation (y-direction) in the trajectory compared to that of Case A. The size (b) and circulation (c) of the starting-jet vortices are similar for Cases A and C. The lateral deviation is more pronounced for Case D, shown in Figure 4.8, which had identified expelled lateral boundary layer vortices for the second and fourth tidal cycles shown in Figure 4.9. Starting-jet vortices in Case D have size (a) and circulation (b) magnitudes 50% smaller than that of Case A.

As the jetty length is further increased for Case E the deviation in the trajectory compared to Case A grows. An expelled boundary layer vortex is identified for the second and third tidal cycles for Case E and is presented in Figure 4.9. A comparison
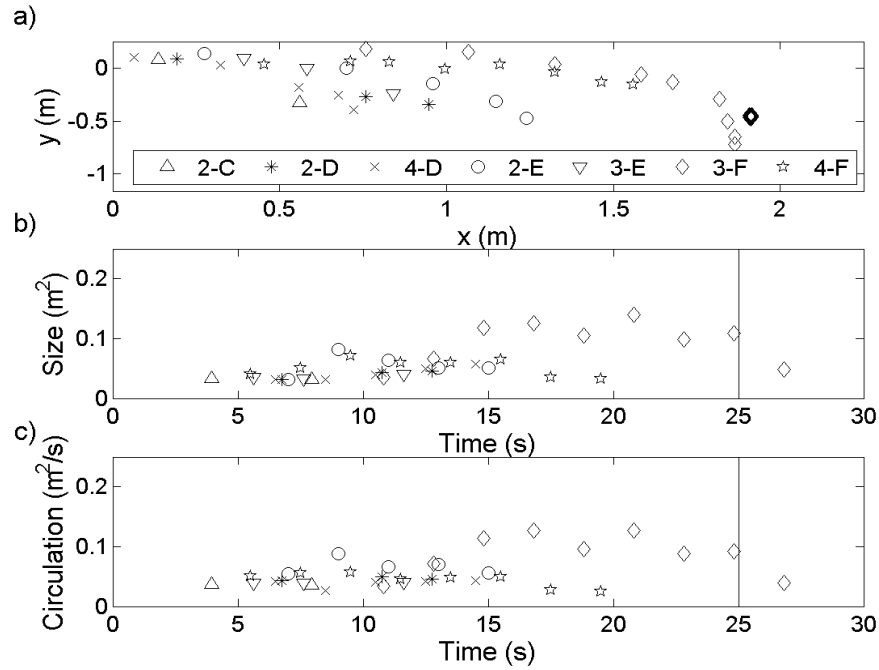
Fig. 4.9.   The trajectory (a), size (b), and circulation (c) of the expelled boundary layer vortices for Cases C, D, E, and F.

between the expelled boundary layer vortices for Cases C, D, E and F show the vortices clearly moving further away from the inlet with increasing jetty length. Though an expelled boundary layer vortex is not found for all the tidal cycles in every case, the vorticity transported out of the channel still changes the starting-jet vortices.

Despite the lateral deviation in the starting-jet vortices' trajectory, the system response for Cases A, C, D, and E is still Mode 0. The clear distinction between Mode 0

and Mode 1A or 1B is that the starting jet vortex in Mode 1A and 1B forms a dipole with the expelled boundary layer, while the starting-jet vortex in Mode 0 forms a dipole with the starting-jet vortex that forms on the opposite side of the channel. As the bifurcation increases (the circulation of the expelled boundary layer vortex becomes larger) with an increase in channel length the system response changes from Mode 0 to either Mode 1A or 1B. Figure 4.10 shows Mode 1A and 1B for the barrier island Case B which has a channel length of 1.35m. Mode 1A is characterized as a vortex system whose trajectory is approximately a 35 degree angle from the origin as the expelled boundary layer vortex and starting-jet vortex form a dipole. The strength of the expelled boundary layer vortex in Mode 1A is significantly less than its starting-jet vortex counterpart.
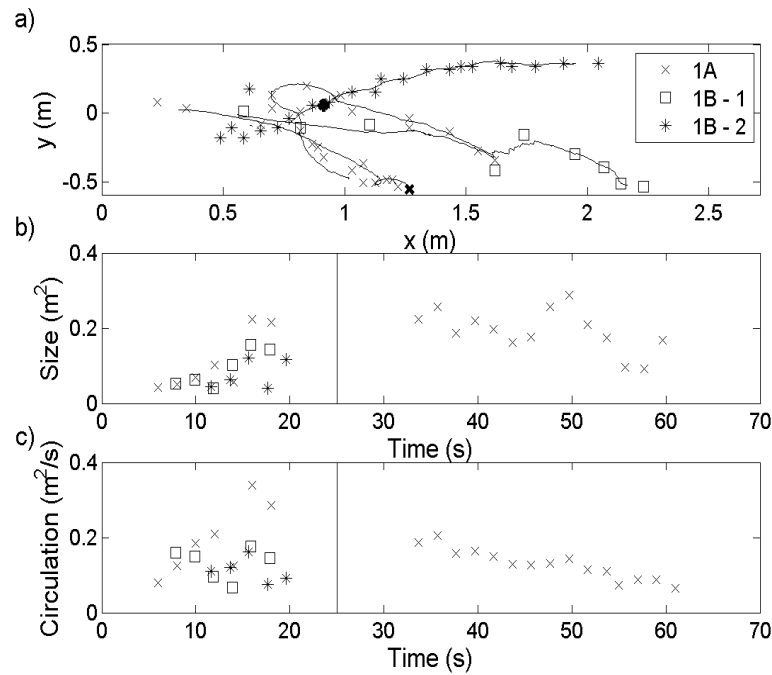
Fig. 4.10. The trajectory (a), size (b), and circulation (c) for a typical Mode 1A and Mode 1B for Case B.

Near the edge of the field of view, the expelled boundary layer is dissipated and downwelled as it joins the starting-jet vortex. Because the starting-jet vortex is on the verge of the field of view, the calculation of the circulation and size is inherently biased low at this point, thus forcing this data to be removed. However, the center of circulation is still visible allowing for the correct trajectory to be calculated. As the tide reverses, the starting-jet vortex is pulled back towards the inlet and is pushed away during the subsequent ebb tide.

For Mode 1B, the starting-jet vortex (vortex 1B-1) quickly forms a dipole with the expelled boundary layer vortex. Because both vortices are roughly the same size and strength, the dipole moves away from the inlet at a 20 degree angle and rapidly out of the field of view. As the dipole propagates away from the inlet, smaller vortices shed from the inlet boundary and organize through inverse cascade to form another large two-dimensional coherent structure whose strength and size are similar to the original starting-jet vortex, vortex 1B-1. The trajectory of this second structure is similar to that of a starting-jet vortex without the influence of a boundary layer vortex (Mode 0). One observation from the experiments is that the growth of the starting-jet vortices for Case B correlate with the time the vortex is still directly attached to the inlet. This time can be defined as a spin-up time and defined quantitatively as the time at which the swirl strength contour detaches from the inlet. However, this is not the sole factor in defining the strength and size of the starting-jet vortices, which are also greatly affected by the capture of secondary vortices. During the first tidal cycle for Case B, the starting-jet vortex has a spin-up time of 13.25 seconds; while in the second, third, and fourth tidal

cycles, the spin-up times are 8, 5.8, and 5.9 seconds, respectively. The data shows similar strengths for the Mode 1A and Mode 1B starting-jet vortices, which is to be expected for spin-up times so closely matched.

Despite the different trajectories between the second, third, and fourth tidal cycles, the expelled boundary layer has an almost identical trajectory, size, and circulation for the second, third, and fourth tidal cycle of Case B shown in Figure 4.11. This is important for two reasons. First, it shows that the conditions within the inlet channel are similar for the second, third, and fourth tidal cycles. Secondly, it means the results shown are not random, but are governed by the interaction between repeatable coherent structures.
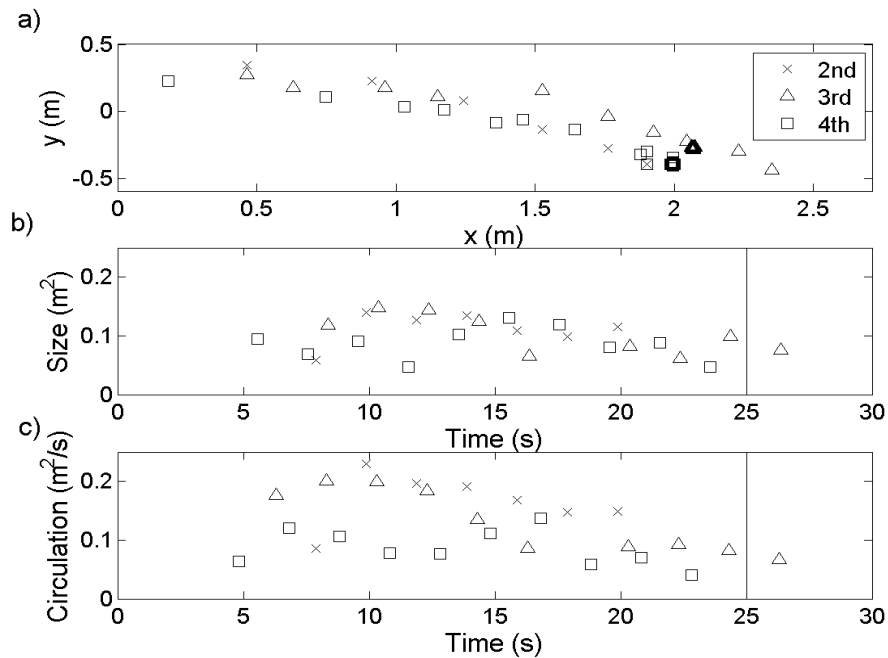
Fig. 4.11. The trajectory (a), size (b), and circulation (c) for the starting-jet vortices for Case B.

The final geometry, Case F, results are presented in Figure 4.12 where the dynamical system response is Mode 1A and 1B. This sudden change between Case E and Case F establishes that at a jetty or channel length between 87 and 111 cm, the bifurcation becomes too large (expelled lateral boundary layer becomes too energetic) thus changing the starting-jet vortices trajectory drastically. The expelled boundary layer vortices for Case F shown in Figure 4.9 show an increase in size and circulation which can be contributed to an increase in the channel length.
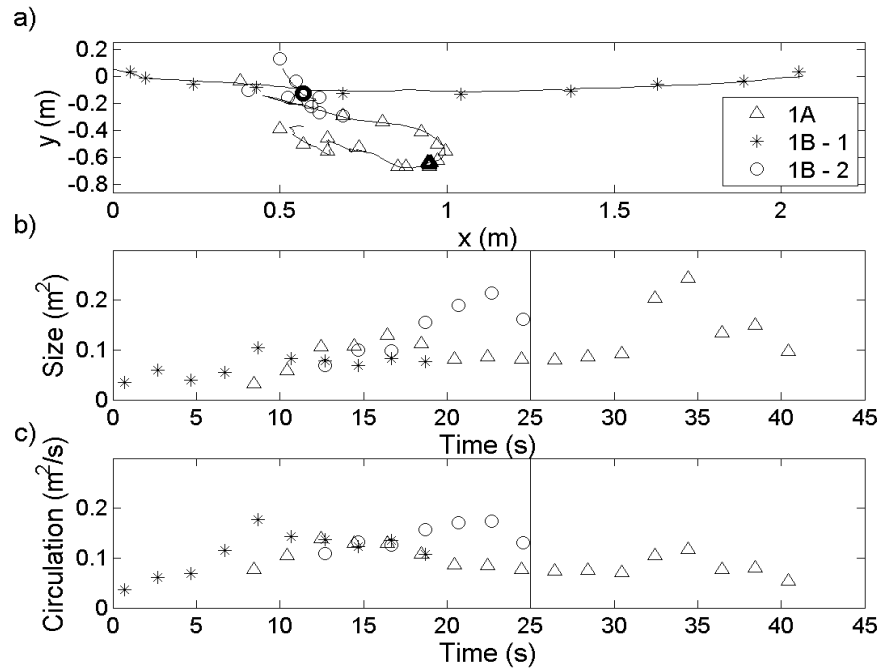
Fig. 4.12. The trajectory (a), size (b), and circulation (c) for a typical Mode 1A and Mode 1B for Case F.

4.4 Discussion

4.4.1 Prediction of Expelled Boundary Layer Vortex

Expelled boundary layer vortices have been shown in the previous section to be very consistent in size and circulation.   Here we develop a model to predict these characteristics.   Consider a boundary layer along a channel with length, L.   This boundary layer has a no-slip condition at the wall and a depth-average velocity of u in the free stream which is a distance δ from the wall. Since the tidal flow is sinusoidal, the average free stream velocity was used, which is calculated as $u = 2U/\pi$. The dominant term in the vorticity is the gradient of the velocity u, $\partial u / \partial y$. Thus the total circulation, Γ_E, in the boundary layer can be seen as

$$\Gamma = \int_0^L \int_0^\delta \frac{\partial u}{\partial y} \partial y \partial x = \int_0^L \int_0^\delta \partial u \partial x = \int_0^L \frac{2U}{\pi} \partial x = \frac{2UL}{\pi} \qquad (4.3)$$

Vortex size can be found as the circulation divided by the average vorticity.   By assuming the boundary layer width to be proportional to the free stream velocity, the average vorticity in the boundary layer is found simply by U/δ. Defining the average vorticity as U/δ requires the need to find the width of the boundary layer, δ, for every experiment. Use of the dye study videos, where dye was injected at the tip of the inlet on the off-shore side of the inlet, made it possible to estimate the width of the boundary layer defined as the distance over which the dye was present. Using this information, a predicted size and circulation of the expelled boundary layer could be found. Figure

4.13 shows the predicted size (a) and circulation (b) of the boundary layer vortices versus the values found using the PIV data.
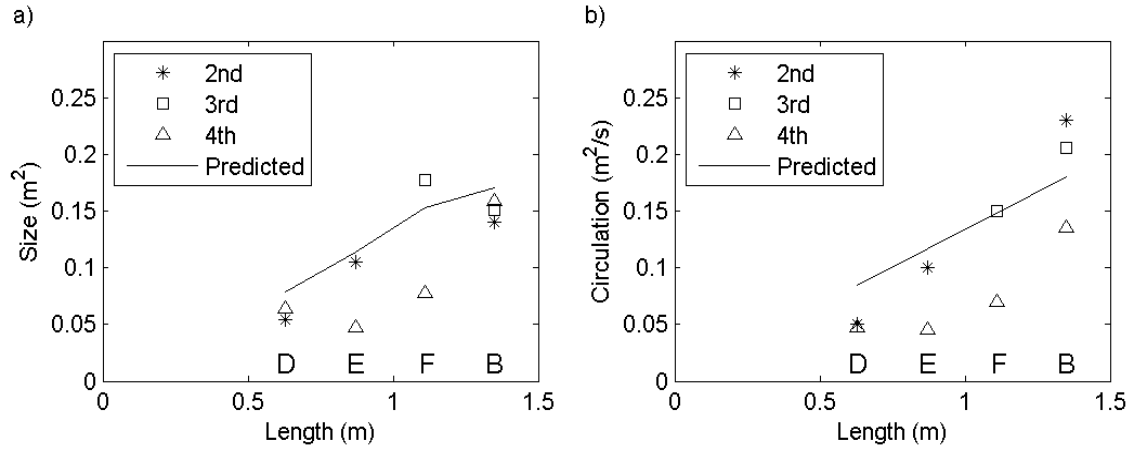
Fig. 4.13.   The size (a) and circulation (b) of the expelled lateral boundary layer vortices versus the length of the channel.

This simple model calculates the size and circulation of the expelled boundary layer vortex with good agreement for all the cases except for two during the fourth tidal cycle. This lack of agreement could be contributed to a reduction in the PIV data quality due to poorer seeding of tracer particles as the experiment runs in time. The above method captures the slope of the data, visualized in Figure 4.13, showing the vortex size and circulation to be linearly proportional with the channel length.

4.4.2 Quantifying the Starting-Jet Vortices with Changes in the Channel Length

The previous section predicted the size and circulation of the expelled lateral boundary layer vortex but did not address how this increase in vortex strength changes the tidal

starting-jet vortices. A maximum starting-jet vortex's circulation, Γ_S, can be predicted at

as $U^2 T/\pi$ by following the model used in Wells and van Heijst (2003) when no expelled

boundary layer is present and accounting for the average velocity due to a sinusoidal

current $u = U \sin(2\pi t / T)$ through the channel. Starting-jet vortices when influenced by

the expelled boundary layer vortices are affected by two separate mechanisms. The first

mechanism is the change in the spin-up time. In this section, only Cases A, C, D, E, and

F are considered since they represent a similar geometry with only the jetty length

changing. Figure 4.14 shows the average spin-up time over tidal cycles 2, 3, and 4 with

the error bars showing the maximum and minimum values versus the increase in channel

length, which is proportional to the strength of the expelled boundary layer vortices. It

can be seen that as the channel length increases the spin-up time decreases. This

supports the hypothesis that the vortex growth is disrupted by the boundary layer vortex.

The change is linear, suggesting the increase in the boundary layer vortex strength is

inversely related to the spin-up time. A comparison between the vortices' average

circulation at the conclusion of the spin-up is shown in Figure 4.15 where the error bars

represent the maximum and minimum values for the data. This figure shows that the

size and circulation is smaller with a shorter spin-up time.
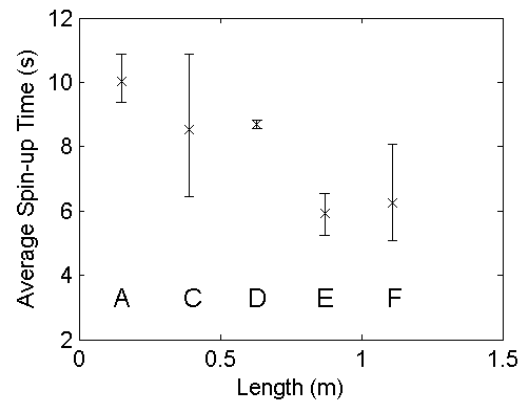
Fig. 4.14. Comparison of the average spin-up time versus the length of the channel for Cases A, C, D, E and F for the second, third and fourth tidal cycles with the error bars showing the maximum and minimum values.
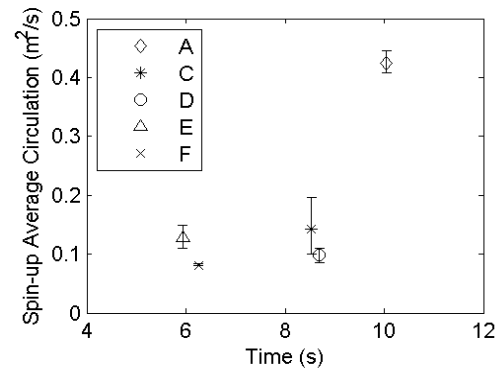
Fig. 4.15. Comparison of the circulation at the end of the spin-up versus the total spin-up time for Cases A, C, D, E and F for tidal cycles two, three, and four with the error bars showing the maximum and minimum values.

Spin-up time alone cannot account for the decrease in the starting-jet vortices' size and circulation, and another mechanism must be identified. The average maximum

circulation compared to the inlet channel length for each experiment is shown in Figure 4.16 with the error bars giving the maximum and minimum values.
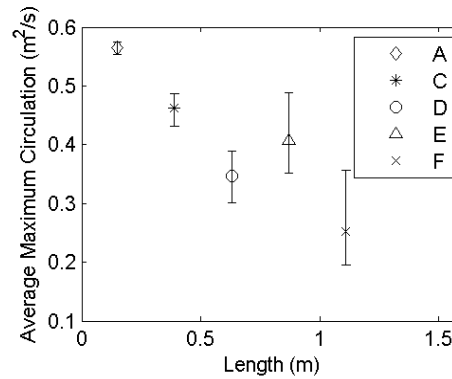
Fig. 4.16. Comparison of the maximum circulation versus the inlet length for Cases A, C, D, E and F for tidal cycles two, three and four with the error bars showing the maximum and minimum values.

This figure clearly shows a decrease in the starting-jet vortices' circulation with an increase in the channel length. A second mechanism accountable for the decrease in the starting-jet vortices' strength lies in how far the starting-jet vortex and boundary layer dipole move from the shear layer of the tidal jet. Shear layer instabilities act to further increase the size and circulation of the starting-jet vortex even after the initial separation from the inlet. The trajectories of the starting-jet vortices for Case A show the vortices moving parallel to the centerline of the inlet channel. This trajectory keeps the starting-jet vortex in the shear layer between the ebb tide jet and the ambient fluid, allowing for the vortex to grow even after propagating away from the inlet exit as secondary instabilities intensify the starting-jet vortex through the inverse cascade, typical in two-dimensional flows.

A comparison between the average maximum lateral distance of the starting-jet vortices from the inlet edge and the channel length is found in Figure 4.17 with the error bars giving the maximum and minimum value. This figure shows that the average maximum lateral distance of the starting-jet vortices and the channel length are proportional for the experimental range tested. Since the expelled boundary layer vortex intensifies with an increased channel length, the lateral deviation from the case without a boundary layer also increases.
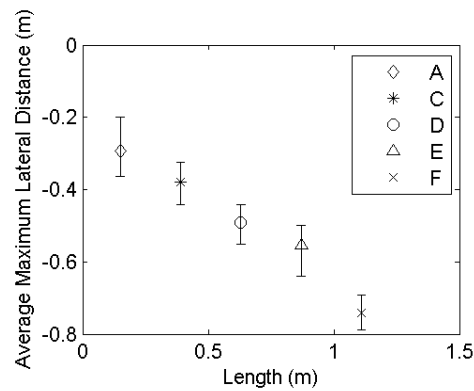
Fig. 4.17. Comparison of the inlet channel length with the average maximum lateral distance (m) for Cases A, C, D, E and F for tidal cycles two, three and four with the error bars showing the maximum and minimum values.

A dipole whose vortices are the same strength and size will move in a straight path. However, the tidal starting-jet vortices are larger and stronger than the expelled boundary layer vortex resulting in a dipole having a curved path, pulling towards the stronger vortex. This difference in vortex strength explains why the trajectory becomes increasingly normal to the inlet centerline with increases in inlet channel length.

The angle of displacement for the starting-jet vortex can be calculated as the arctangent of the ratio of the maximum lateral distance (y) to the corresponding streamwise distance (x). The average angle of vortex displacement in comparison to the ratio of the two predicted circulations, Γ_E to Γ_S, is shown in Figure 4.18, showing the angle of vortex displacement growing (Cases A to E) as the channel length is increased for the system response Mode 0 to a maximum value of 50 degrees. However, the angle for Mode 1A and 1B are smaller, where Mode 1B has an angle of vortex displacement similar to the shortest experimental channel length (Case A). This figure shows that the change from Mode 0 to Mode 1 occurs at a *2L/UT* value of approximately 1/5, meaning the predicted starting jet vortex circulation is five times stronger than the expelled boundary layer circulation. A value *2L/UT* less than 1/5 results in a dynamical response of Mode 0 response while a value greater than 1/5 is Mode 1.
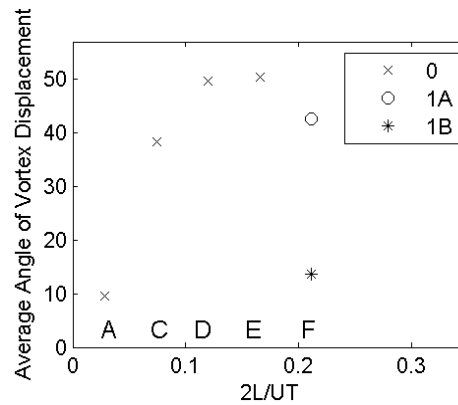
Fig. 4.18.   Average angle of vortex displacement compared to the inlet length for Mode 0, 1A, and 1B for Cases A, C, D, E, and F.

4.5 Concluding Remarks

Surface particle image velocimetry (PIV) was used to investigate tidal starting-jet vortices influenced by expelled lateral boundary layer vortices. The resulting continuous velocity fields were processed using local swirl strength criteria to identify and quantify the trajectory, size, and circulation of large two-dimensional coherent structures. Results were presented showing the trajectory, size, and circulation of the starting-jet vortices and expelled lateral boundary layer vortices for all the experiments and tidal cycles. The figures show an increase in the lateral deviation in the trajectory of the starting-jet vortices and a decrease in the starting-jet vortex size and circulation corresponding with an increase in the inlet channel length. Using these quantities, an understanding of the mechanics between the starting-jet vortices and expelled lateral boundary vortices were found and quantified.

A model was developed to predict the strength of the expelled boundary layer vortex; however, this model does not account for frictional effects and vortex stretching which will reduce the size and strength. The expelled boundary layer was found to change the starting-jet vortices through two mechanisms. The first was to reduce the spin-up time, the time before the vortex separates from the inlet. The second was to form a dipole, further distancing the starting-jet vortex from the shear layer where smaller instabilities can continue to contribute to the large two-dimensional structure through the inverse energy cascade. This study has explained the mechanisms responsible for changes to starting-jet vortices due to an expelled boundary layer and

offered a predictor value of 5 for the quantity *UT/2L* that represents a change in the dynamical system response from Mode 0 to either Mode 1A or 1B.

CHAPTER V

CONCLUSIONS

5.1 Summary

This dissertation has presented the results of PIV investigations of multiphase plumes and tidal vortices with emphasis on the identification and quantification of vortices in the flow. This chapter will summarize the findings of each PIV investigation and discuss the overarching goals of this dissertation and recommendations for future studies.

In Chapter II, an investigation into the turbulence of bubble plumes was conducted using PIV (Bryant et al. 2009). This chapter used the local swirl strength to identify vortices in the flow and developed a method to quantify the location, size, circulation, and enstrophy of these identified vortices. The results of this section showed in the studied buoyancy fluxes, the bubble plumes' mean and turbulent properties were self-similar when nondimensionalized by the centerline velocity v_c and plume radius r with the velocity profiles matching a Gaussian distribution The average and maximum identified vortices where largest along the plume edge which corresponded to the region of highest vorticity. For the bubble plumes this was also along the edge of the dispersed phase as the value of lambda was 0.77 to 0.91 for the measured buoyancy fluxes. Furthermore, the most energetic vortices were also along the plume edge.

Beyond the calculations of vortex properties, the turbulent stresses were found to be self-similar when nondimensionalized by the local velocity, $v(x)$. The integral length scale, L_1, was found to be in agreement with the largest vortices found in the flow. This

agreement between the integral length scale and the maximum vortex size confirmed the method of identifying and quantifying turbulent structures spatially. The turbulent energy spectra were found to have a reduced slope of -7/6 in the inertial subrange, agreeing with that found in other bubbly flows.

The investigation of nine different inertial particle plumes was presented in Chapter III. This chapter also used the techniques developed in Chapter II and compared its results to that of bubble plumes. Like the bubble plume data presented in Chapter II, the results were nondimensionalized using the time-averaged centerline velocity $\underline{v_c}$ and plume radius r; however, unlike the bubble plumes, the average vortex results did not collapse for the 1.0 mm size particles. The time-averaged velocity and vorticity profiles were self-similar with the maximum vorticity region occurring at half the plume radius. This also marked the region where the dispersed phase core ended. Unlike the bubble plume, the inertial particle plumes had values on the order of 0.5. This smaller lambda, along with the increasing intermittency due to particle drafting and swarming, allow for much large vortices to form in the 2.0 and 1.45 mm cases. The maximum and average vortex size occurred at half the plume radius, while the most energetic vortices occurred in the particle plume core. In general, the 1.0 mm particle size plumes had the closest agreement with the bubble plume data.

The calculation of time average turbulent stress showed the particle plumes to have a higher vertical stress than a bubble plume. This difference can be associated with the mass and boundary layer of the particles. However, like the bubble plume data, the

turbulent energy spectra showed the same -7/6 in the inertial subrange of the dispersed phase region of the plume.

Chapter IV quantified the effect of a finite channel length on the development and production of tidal vortices. The method of identification and quantification for tidal vortices developed in Chapter II was expanded to track large two-dimensional structures. First, this chapter showed that for cases of simple geometry, the tidal vortices development and trajectory becomes quasi steady state in the second tidal cycle. The results also showed that as the channel length increases, the size and circulation of the starting-jet vortices decreases. Investigating this decrease in size and circulation showed the expelled lateral boundary layer vortex became larger in size and circulation with an increase in channel length. The expelled vortices whose circulation was opposite that of the starting-jet vortices formed dipoles whose trajectory moved the starting-jet vortex away from the channel inlet and shear layer. This separation from the tidal jet's shear layer severed the input energy needed for growth, thus, reducing its size and circulation. This investigation also found that when the ratio between the expelled lateral boundary layer vortices and starting-tidal jet vortices circulation was 1/5, the system dynamics changed from Mode 0 to a two-state Mode 1. Mode 1 was characterized by two different trajectories. The first trajectory is characterized with the tidal starting-jet vortices moving quickly away from the inlet at a 40 to 50 degree angle before drawing back towards the inlet from the flood tide. In the second observed trajectory in Mode 1, the expelled boundary layer formed a dipole with the starting-jet vortex early in its development. This resulted in a more symmetric dipole whose trajectory was a much

milder angle (~20 degrees). This dipole moved away early in the ebb tide allowing for the development of an additional tidal vortex along the tidal jet shear layer by the inverse cascade of smaller vortices.

This dissertation has used vortex identification and quantification methods to successfully describe the mean and turbulent properties of three different flows: bubble plumes, tidal vortices, and inertial particle plumes. The knowledge gained from this dissertation should assist engineers in numerous applications including reservoir aeration, CO_2 sequestration, estuary flushing, and industrial mixing.

5.2 Recommendations

In concluding this dissertation the following section will make recommendations for the continuation of the research presented. The developed vortex identification and quantification scheme used in this dissertation can be applied to a variety of other problems with particular focus on the understanding of sediment transport. In addition, the tracking developed for the study of tidal starting-jet vortices could aid in the study of vortex creation and dissipation in a variety of suitable flow fields. In addition to these general comments for future research, a list of more specifics recommendations follow.

- The bubble plume experiments presented in this dissertation used an airstone diffuser that produced similar size bubbles for all the air flow rates tested; however, the size of the bubbles should be an important parameter in the generation and properties of the turbulence in bubble plumes. Different bubble sizes could be accomplished by using a diffuser that uses hypodermic needles of

different diameters such as that of Sun and Faeth (1986). Furthermore, by adjusting the bubble size it may be possible to determine the mechanism for the observed modulation of the turbulent energy spectra in both the bubble and inertial particle plume. In addition to controlling the bubble size, the coupling of hot film anemometry and high-speed PIV could detail whether this modulation is a result of the acceleration of fluid around the dispersed phase or vortex shedding. This knowledge would allow for engineers to choose the size of bubbles or particles to have the desired turbulent energy spectra properties such as increased dissipation.

- Lastly inertial particle plume experiments conducted in a stratified ambient would allow for a greater understanding of multiphase plumes in the ocean, which would be paramount to the design of CO_2 sequestration plumes. This research could be conducted in a laboratory using PIV with stratification being achieved using salt and ethanol. In addition to conducting experiments in stratification, a gradation of particle sizes could be also used to better understand sediment plumes whose particles would have a grain size distribution.

- The influence of longshore currents on the development and trajectory of tidal starting-jet vortices is important to investigate as these currents would generate vorticity that could enhance or dampen the tidal starting-jet vortices. In addition, to vorticity generated from longshore currents, the Coriolis effect would either

enhance or dampen the tidal vortices depending on the rotation and hemisphere. These two conditions are difficult to model in the lab, instead requiring the use of numerical models such as ADCIRC or COULWAVE. However, the results presented herein could used to calibrate those models. Lastly, the effect of stratification on the development of starting-jet vortices would be of great interest since the water in the tidal jet during the ebb tide will have a lower density than that of the ocean. Stratification would dampen any vertical turbulence associated with the large two dimensional structures. Stratification experiment could be conducted in the lab or using a numerical model with a range of Richardson Numbers to determine its effects.

REFERENCES

Adams, E. E., and Wannamaker, E. J. (2005). "Dilution strategies for direct ocean carbon sequestration." *J. Mar. Environ. Eng.*, 8, 95-109.

Adams, E. E., and Wannamaker, E. J. (2006). "Modeling descending carbon dioxide injections in the ocean." *J. Hydraul. Res.*, 44, 324-337.

Adrian, R. J., Christensen, K. T., and Liu, Z. C. (2000). "Analysis and interpretation of instantaneous turbulent velocity fields." *Exp. Fluids*, 29**,** 275-290.

Asaeda, T., and Imberger, J. (1993). "Structure of bubble plumes in linearly stratified environments." *J. Fluid Mech.*, 249**,** 35-57.

Baines, W. D., and Leitch, A. M. (1992). "Destruction of stratification by bubble plume." *J. Hydraul. Eng.*, 118, 559-577.

Balachandar, S. (2009). "A scaling analysis for point-particle approaches to turbulent multiphase flows." *Int. J. Multiphas. Flow*, 35, 801-810.

Becker, S., De Bie, H., and Sweeney, J. (1999). "Dynamic flow behavior in bubble columns." *Chem. Eng. Sci.*, 54, 4929-4935.

Bolotnov, I. A., Lahey Jr., R. T., Drew, D. A., and Jansen, K. E. (2008). "Turbulent cascade modeling of single and bubbly two-phase flows." *Int. J. Multiphas. Flow*, 34**,** 1142-1151.

Bombardelli, F. A., Buscaglia, G. C., and García, M. H. (2003). "Parallel computations of the dynamic behavior of bubble plumes." *Pressure Vessels and Piping Conference*, ASME, Cleveland, Ohio, 185-201.

Bombardelli, F. A., Buscaglia, G. C., Rehmann, C. R., Rincón, L. E., and García, M. H. (2007). "Modeling and scaling of aeration bubble plumes: a two-phase flow analysis." *J. Hydraul. Res.,* 45**,** 617-630.

Brenn, G., Braeske, H., and Durst, F. (2002). "Investigation of the unsteady two-phase flow with small bubbles in a model bubble column using phase-Doppler anemometry." *Chem. Eng. Sci.*, 57, 5143-5159.

Bryant, D. B., Seol, D.-G., and Socolofsky, S. A. (2009). "Quantification of turbulence properties in bubble plumes using vortex identification methods." *Phys. Fluids*, 21, 075101.

Buscaglia, G. C., Bombardelli, F. A., and García, M. H. (2002). "Numerical modeling of large-scale bubble plumes accounting for mass transfer effects." *Int. J. Multiphas. Flow*, 28**,** 1763-1785.

Buwa, V. V., and Ranade, V. V. (2002). "Dynamics of gas-liquid flow in a rectangular bubble column: experiments and single/multi-group CFD simulations." *Chem. Eng. Sci.*, 57, 4715-4736.

Chadwick, D. B., and Largier, J. L. (1999a). "The influence of tidal range on the exchange between San Diego Bay and the ocean." *J. Geophys. Res. – Oceans*, 104, 29885-29899.

Chadwick, D. B., and Largier, J. L. (1999b). "Tidal exchange at the bay-ocean boundary." *J. Geophys. Res. – Oceans*, 104, 29901-29924.

Clift, R., Grace, J. R., and Weber, M. E. (1978). *Bubbles, Drops, and Particles*, Academic Press, New York.

del Roure, F. N. (2007). "Laboratory studies of eddy structures and exchange processes through tidal inlets." M.S. thesis, Texas A&M University, College Station, TX.

del Roure, F. N., Socolofsky, S. A., and Chang, K. –A. (2009). "Structure and evolution of tidal starting-jet vortices at idealized barotropic inlets," *J. of Geophs.Res.– Oceans*, 114, C05024.

Díaz, M. E., Montes, F. J., and Galán, M. A. (2006). "Influence of aspect ration and superficial gas velocity on the evolution of unsteady flow structures and flow transitions in a rectangular two-dimensional bubble column." *Ind. Eng. Chem. Res.*, 45, 7301-7312.

García, C. M., and García, M. H. (2006). "Characterization of flow turbulence in large-scale bubble-plume experiments." *Exp. Fluids*, 41, 91-101.

Geyer, R. W. (1993). "Three-dimensional tidal flow around headlands." *J. Geophys. Res. – Oceans*, 98, 955-966.

Geyer, R. W., and Signell, R. (1990). "Measurements of tidal flow around a headland with a shipboard acoustic Doppler profiler." *J. of Geophys. Res. – Ocean*, 95, 3189-3197.

Holmes, P., Lumley, J., and Berkooz, G. (1996). *Turbulence, Coherent Structures, Dynamical Systems and Symmetry*, Cambridge University Press, New York.

Jirka, G. H. (2001). "Large scale flow structures and mixing process in shallow flows." *J. Hydraul. Res.*, 39(6), 567-573.

Kashiwai, M. (1985a). "TIDICS-control of tidal residual circulation and tidal exchange in a channel-basin system." *J. of Oceanographical Society of Japan*, 41, 1-10.

Kashiwai, M. (1985b). "A hydraulic experiment on tidal exchange." *Journal of the Oceanographical Society of Japan*, 41, 11-24.

Khalitov, D. A., and Longmire, E. K. (2002). "Simultaneous two-phase PIV by two-parameter phase discrimination." *Exp. Fluids*, 32(2), 252-268.

Kim, D. H., Lynett, P. J., and Socolofsky, S. A. (2009). "A depth-integrated model for weakly dispersive, turbulent, and rotational flows." *Ocean Model.*, 27, 198-214.

Lance, M., and Bataille, J. (1991). "Turbulence in the liquid phase of a uniform bubbly air-water flow." *J. Fluid Mech.*, 222**,** 95-118.

LaVision GmbH, (2002). *DaVis FlowMaster Software for DaVis 6.2.*, LaVision GmbH, Goettingen, Germany.

Lemckert, C. J., and Imberger, J. (1993). "Energetic bubble plumes in arbitrary stratification." *J. Hydraul. Eng.*, 119, 680-703.

Lin, J. –C., Ozgoren, M., and Rockwell, D. (2003). "Space time development of the onset of a shallow-water vortex." *J. Fluid Mech.*, 485, 33-66.

Lophaven, S. N., Nielsen, H. B., and Søndergaard, J. (2002). *DACE: a Matlab Kriging Toolbox*, Technical University of Denmark, Lyngby.

Mathieu, J., and Scott, J. (2000). *An Introduction to Turbulent Flow*, Cambridge University Press, Cambridge.

McDougall, T. J. (1978). "Bubble plumes in stratified environments." *J. Fluid Mech.*, 85**,** 655-672.

McGinnis, D. F., Lorke, A., Wuest, A., Stockli, A., and Little, J. C. (2004). "Interaction between a bubble plume and the near field in a stratified lake." *Water Resour. Res.*, 40, W10206.

Metz, B., Davidson, O., de Coninck, H., Loos, M., and Meyer, L. (2005). *Carbon Dioxide Capture and Storage*. Intergovernmental Panel on Climate Change, Cambridge University Press, Cambridge.

Meyer, K. E., Pedersen, J. M., and Özcan, O. (2007). "A turbulent jet in crossflow analysed with proper orthogonal decomposition." *J. Fluid Mech.*, 583, 199-227.

Milgram, J. H. (1983). "Mean flow in round bubble plumes." *J. Fluid Mech.*, 133, 345-376.

Mudde, R. F., Groen, J. S., and Van Den Akker, H. E. A. (1997). "Liquid velocity field in a bubble column: LDA experiments." *Chem. Eng. Sci.*, 52, 4217-4224.

Mudde, R. F., and Van Den Akker, H. E. A. (1999). "Dynamic behavior of the flow field of a bubble column at low to moderate gas fractions." *Chem. Eng. Sci.*, 54, 4921-4927.

Old, C. P., and Vennell, R. (2001). "Acoustic Doppler current profiler measurements of the velocity field of an ebb tidal jet." *J. Geophys. Res. – Ocean*, 106, 7037-7049.

Pawlak, G., MacCready, P., Edwards, K. A., and McCabe, R. (2003) "Observations on the evolution of tidal vorticity at a stratified deep water headland." *Geophys. Res. Lett. – Ocean*, 30(24), 2234.

Pope, S. B. (2000). *Turbulent Flow*, Cambridge University Press, New York.

Raffel, M., Willert, C. E., and Kompenhans, J. (1998). *Particle Image Velocimetry: A Practical Guide*, Springer, New York.

Rensen, J., Luther, S., and Lohse, D. (2005). "The effect of bubbles on developed turbulence." *J. Fluid Mech.*, 538, 153-187.

Rensen, J., and Roig, V. (2001). "Experimental study of the unsteady structure of a confined bubble plume." *Int. J. Multiphas. Flow*, 27, 1431-1449.

Roughan, M., Mace, A. J., Largier, J. L., Morgan, S. G., Fisher, J. L., and Carter, M. L. (2005). "Subsurface recirculation and larval retention in the lee of a small headland: a variation on the upwelling shadow theme." *J. Geophys. Res. – Ocean*, 110, C10027.

Seol, D.-G., Bhaumik, T., Bergmann, C., and Socolofsky, S. A. (2007). "Particle image velocimetry measurements of the mean flow characteristics in a bubble plume." *J. Eng. Mech.*, 133, 665-676.

Seol, D.-G., and Socolofsky, S. A. (2008). "Vector post-processing algorithm for phase discrimination of two-phase PIV." *Exp. Fluids*, 45, 223-239.

Shawkat, M. E., Ching, C. Y., and Shoukri, M. (2007). "On the liquid turbulence energy spectra in two-phase bubbly flow in a large diameter vertical pipe." *Int. J. Multiphas. Flow*, 33, 300-316.

Signell, R. P., and Geyer, W. R. (1991). "Transient eddy formation around headlands." *J. Geophys. Res. – Ocean*, 96, 2561-2575.

Simiano, M., Zboray, R., de Cachard, F., Lakehal, D., and Yadigaroglu, G. (2006). "Comprehensive experimental investigation of the hydrodynamics of large-scale, 3D, oscillating bubble plumes." *Int. J. Multiphas. Flow*, 32, 1160-1181.

Socolofsky, S. A. (2001). "Laboratory experiments of multi-phase plumes in stratification and crossflow." Ph.D. Thesis, Massachusetts Institute of Technology, Cambridge, MA.

Socolofsky, S. A., and Adams, E. E. (2005). "Role of slip velocity in the behavior of stratified multiphase plumes." *J. Hydraul. Eng.*, 131, 273-282.

Soga, C. L. M., and Rehmann, C. R. (2004). "Dissipation of turbulent kinetic energy near a bubble plume." *J. Hydraul. Eng.*, 130, 441-449.

Sun, T. Y., and Faeth, G. M. (1986). "Structure of turbulent bubbly jets. 1. Methods and centerline properties." *Int. J. Multiphas. Flow*, 12(1), 99-114.

Tekeli, S., and Maxwell, W. H. C. (1978). "Behavior of air bubble screens." *Technical Report No. 33*, University of Illinois at Urbana-Campaign, Urbana, IL.

Tennekes, H., and Lumley, J. L. (1972). *A First Course in Turbulence,* MIT Press, Cambridge, Massachusetts.

Van Senden, D. C., and Imberger, J. (1990). "Effects of initial conditions and Ekman suction on tidal outflows from inlets." *J. Geophys. Res. – Ocean*, 95, 13373-13391.

Wain, D. J., and Rehmann, C. R. (2005). "Eddy diffusivity near bubble plumes." *Water Resour. Res.*, 41, W09409.

Wells, M. G., and van Heijst, G. F. (2003). "A model of tidal flushing of an estuary by dipole formation." *Dynam. Atmos. Oceans*, 37, 223-244.

VITA

Duncan Burnette Bryant received his Bachelor of Science degree in civil engineering in 2005 and Master of Science in 2006 from Clemson University. In August of 2006 he began studying ocean engineering pursuing his doctoral degree at Texas A&M University, graduating in May of 2010. His research interests include environmental engineering, laboratory methods to study fluid flows, and the turbulence and coherent structures of multiphase and shallow water flows. He plans to pursue a career in engineering education and research.

Dr. Bryant may be reached at: Coastal and Ocean Engineering Division, Department of Civil Engineering, Texas A&M University, 3136 TAMU, College Station, TX 77843-3136. His email is duncan.bryant@gmail.com.